

A coupled meshless-SBFEM-FEM approach in simulating soil-structure interaction with cross-scale model

Jin Gong^{a,b}, Degao Zou^{a,b,*}, Xianjing Kong^{a,b}, Jingmao Liu^{a,b}, Kai Chen^{a,b}

^a The State Key Laboratory of Coastal and Offshore Engineering, Dalian University of Technology, Dalian, Liaoning, 116024, China

^b School of Hydraulic Engineering, Dalian University of Technology, Dalian, Liaoning, 116024, China

ARTICLE INFO

Keywords:

Multilevel cross-scale model
Meshless interface
Meshless-SBFEM-FEM
Soil-structure interaction
Metro structure

ABSTRACT

This paper presents an integrated, customized routine that uses object-oriented programming and a “super element class” to apply an integrated approach to simulate soil-structure interaction (SSI) problems. The scaled boundary finite element method (SBFEM) and finite element method (FEM) are applied together with the quad tree technique to implement cross-scale modeling for solid elements. Meanwhile, the meshless interface seamlessly connects mismatched and differing sizes of meshes between the soil and the structure, thus allowing cross-scale modeling at the interface level. In addition, through modify the radial point interpolation function (RPIM) and the method of searching supporting nodes, the precision near the boundaries of meshless interface are improved, and circular (cambered) type interfaces can be simulated. Thus, through a coupled Meshless-SBFEM-FEM approach, a fine analysis of soil-structure interaction problem with multilevel cross-scale model can be conducted.

1. Introduction

In a phenomenon called the contact problem, the combined effects of inner and exterior loads can cause uncoordinated deformation between regions of different media. In practical geotechnical engineering, the phenomenon exists extensively in structure-structure contact problems [1], structure-soil contact problems [2], and soil-soil contact problems [3]. Due to the significant difference in mechanical characteristics, the interface between soil and structure may open, close and slip [4], etc. under static and dynamic loads. The structure-soil contact problems are the most important and complex among the listed problems. In addition, in numerical analysis methods such as finite element modeling, a reasonable simulation must carefully consider the interface zones in SSI problems.

The ability to obtain a high-accuracy response of a structure is of great importance in SSI problems, and such a high-accuracy response is accomplished through the use of fine meshes in structure zone. With the conventional FE model, the refined structural meshes can greatly increase the number of elements throughout the entire model, which may decrease computational efficiency. In previous papers, several approaches have been presented to attack this issue. One widely used method is to gradually increase the mesh density as one gets closer to the

interface [5]. However, this method requires excessive manual intervention and is not suitable for 3D modeling. Zhang and Song [6,7] applied the SBFEM-FEM to simulate the progressive damage of structures. Chen et al. presented an optional method that couples SBFEM [8–11] and quad trees to achieve cross-scale modeling and extended their usage to nonlinear materials. The above researchers aimed at achieving cross-scale modeling in solid elements (soil and structure).

In addition, the contributions to the interface are achieved include simulating the interface zone with Goodman elements with zero thickness or finite thickness [3] or with thin finite elements [12,13] as proposed by Desai et al. Since the interface element (i.e. Goodman element and thin finite element) can work with various constitutive models [15–18] to capture the complex soil-structure interaction, the interface element is widely applied to practical geotechnical engineering [2,19,20]. However, the interface elements mentioned above require that the nodes on each side of the interface to be strictly matched. This node-to-node interface element can bring significant restrictions to solving SSI problems. Xing and Song [21,22] presented an SFBEM-based method to convert non-matching node interfaces into node-to-node interfaces for 2D and 3D frictional contact problems. However, the nodal insertion can sometimes complicate modeling operations, especially for 3D models. Meanwhile, this method cannot employ elastic-plastic

* Corresponding author. School of Hydraulic Engineering, Dalian University of Technology, Dalian, Liaoning, 116024, China.

E-mail address: zoudegao@dlut.edu.cn (D. Zou).

<https://doi.org/10.1016/j.soildyn.2020.106214>

Received 9 September 2019; Received in revised form 8 April 2020; Accepted 4 May 2020

Available online 10 June 2020

0267-7261/© 2020 Elsevier Ltd. All rights reserved.

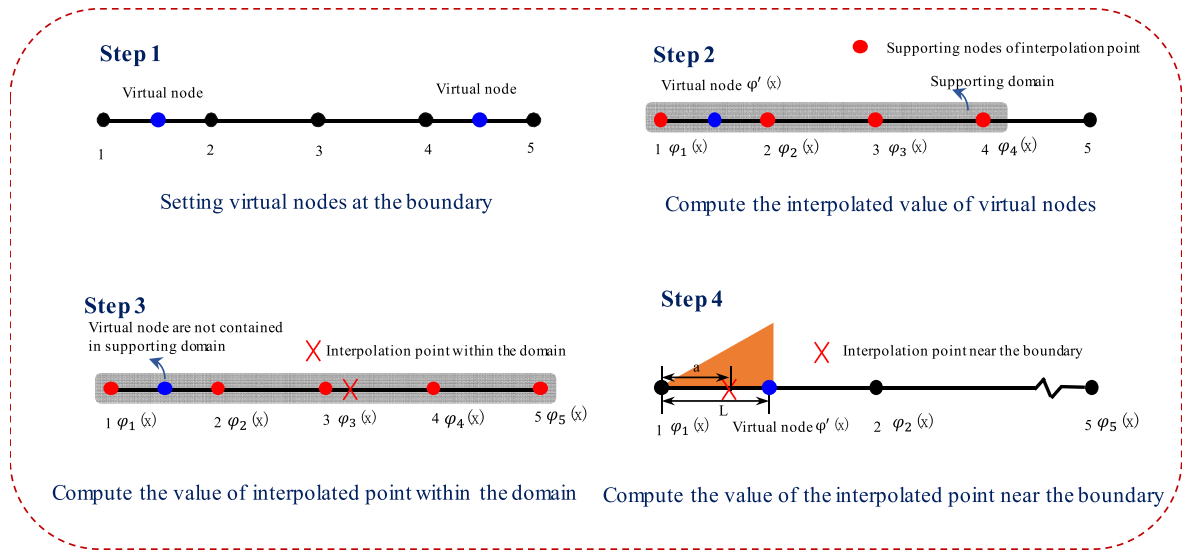


Fig. 1. The process of modified RPIM interpolation function.

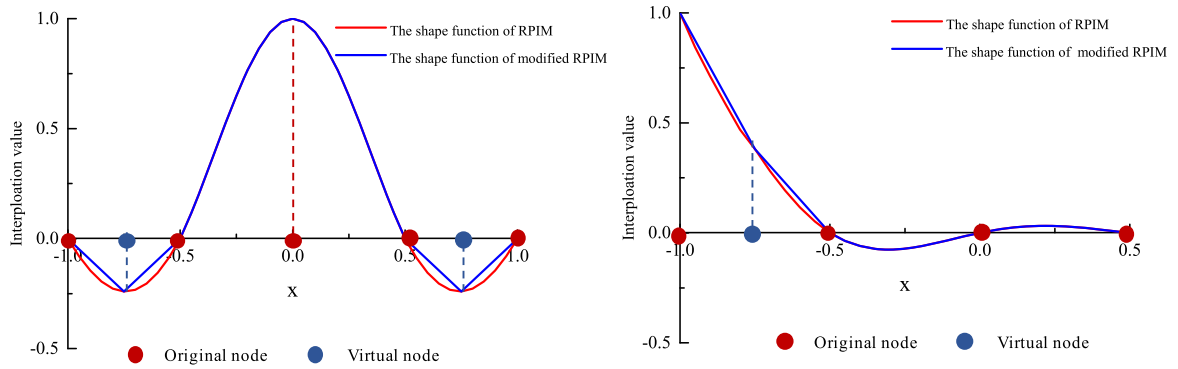


Fig. 2. The comparison of shape functions (modified RPIM vs RPIM).

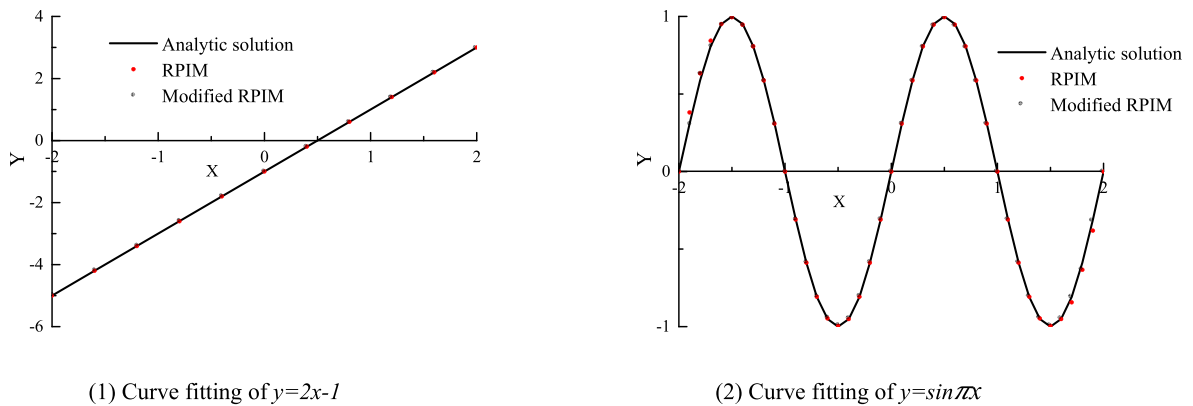
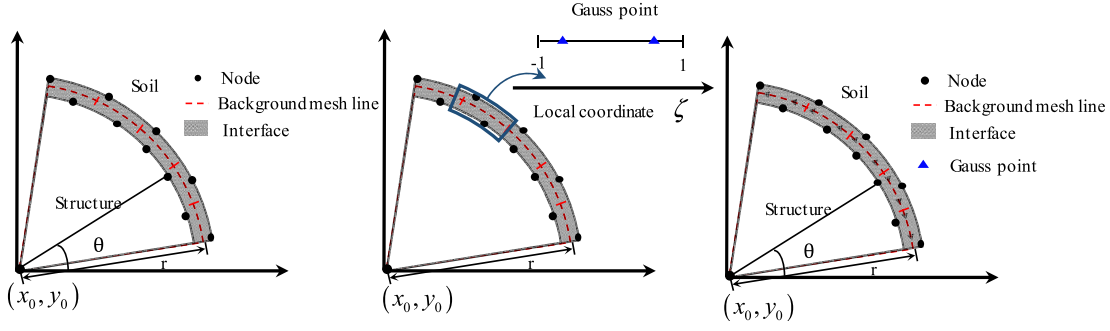


Fig. 3. The comparison of fitted curves (modified RPIM vs RPIM).

interface constitutive models. An interface model with asymmetric nodes was developed by Qu et al. [23,24] and successfully applied in concrete face rock-fill dams (CFRDs). This approach also requires partly matching nodes at the boundary of each interface element. Gong et al. extended the meshless method [25–27] to interface zones. Through introducing the RPIM function [28–30], a non-matching node interface

was achieved to effectively simulate soil-structure interactions [31].

However, the above meshless interface can only be applied to linear shape interfaces at this stage and the precision significantly decreases near boundaries due to the lower density of nodes in the supporting domain of gauss points near boundaries, which will be further discussed in the following sections. In this paper, an enhanced meshless interface



(1) Introduce circular types' background mesh (2) Set gauss points in local coordinates (3) Transform the gauss points to global coordinates

Fig. 4. Generation of gauss points in a background mesh line.

- (2) The method to search for nodes in the supporting domain of each gauss point is improved. Instead of relying on the distance between the gauss point and the nodes, the criteria of searching for nodes in the supporting domain is the radius of the arc formed by the gauss point and the nodes as shown in Fig. 5. The derivation is as follows,

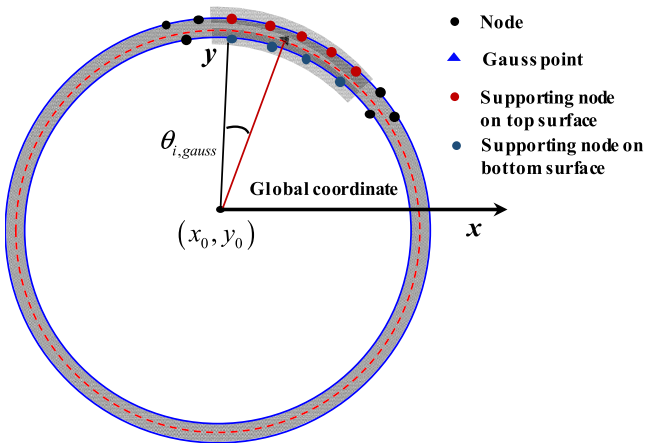


Fig. 5. The modified method to search for nodes in the supporting domain.

is developed to overcome the disadvantages mentioned above through: (1) Introducing circular type background mesh lines to satisfy the interface shape and modifying the searching method to extend the method towards application to circular (cambered) type interfaces. (2) Adding virtual nodes near the edge of interfaces and combining the linear interpolation to produce a significant improvement in accuracy near the boundaries of interfaces.

In this paper, SBFEM is applied to achieve the cross-scale modeling in solid elements [8–11], and the enhanced meshless interfaces can connect soil and structure models that possess different sizes of meshes, which can achieve cross-scale modeling at the interface level [31].

Together with the above techniques, a multilevel cross-scale model can be established, which is of great significant in refined analysis. However, due to different approaches in solving shape functions, stiffness matrices, internal and external force vectors across each method, it is challenging to achieve a coupling of the methods and none papers have coupled the above three methods to solve SSI problems. However, through object-oriented programming and the “super element class”, the SBFEM and the meshless interface can be integrated into the custom developed FEM platform described in this paper. Thus, a highly flexible and effective method that enables a coupled Meshless-SBFEM-FEM approach is presented to implement multilevel, cross-scale modeling for SSI problems. The introduced method is also effective for independent meshing and local mesh optimization problems.

The remainder of this paper is organized as follows. The derivation and numerical implementation of Meshless-SBFEM-FEM is shown in section 2. Two numerical examples are presented in sections 3.1 and 3.2 to verify the improved performance of the enhanced meshless interface. In sections 3.3 and 3.4, the enhanced meshless interface coupled with FEM and SBFEM is applied to the simulation of metro structures (e.g. frame metro station, three-arch column type metro station) for fine damage analysis. Finally, section 4 summarizes the major conclusions in this paper.

2. Coupled Meshless-SBFEM-FEM

The coupled Meshless-SBFEM-FEM is effective in SSI problem, and in this section, the implementation of the coupled method is presented. The derivation of formulas used in the approach is detailed in section 2.1. The computation of element matrices and vectors with enhanced meshless interfaces and SBFEM is summarized in sections 2.2 and 2.3.

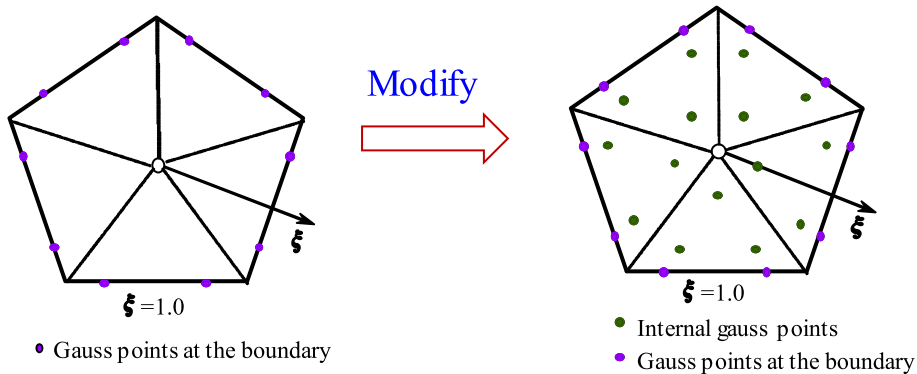


Fig. 6. Introduction of internal gauss points in SBFEM.

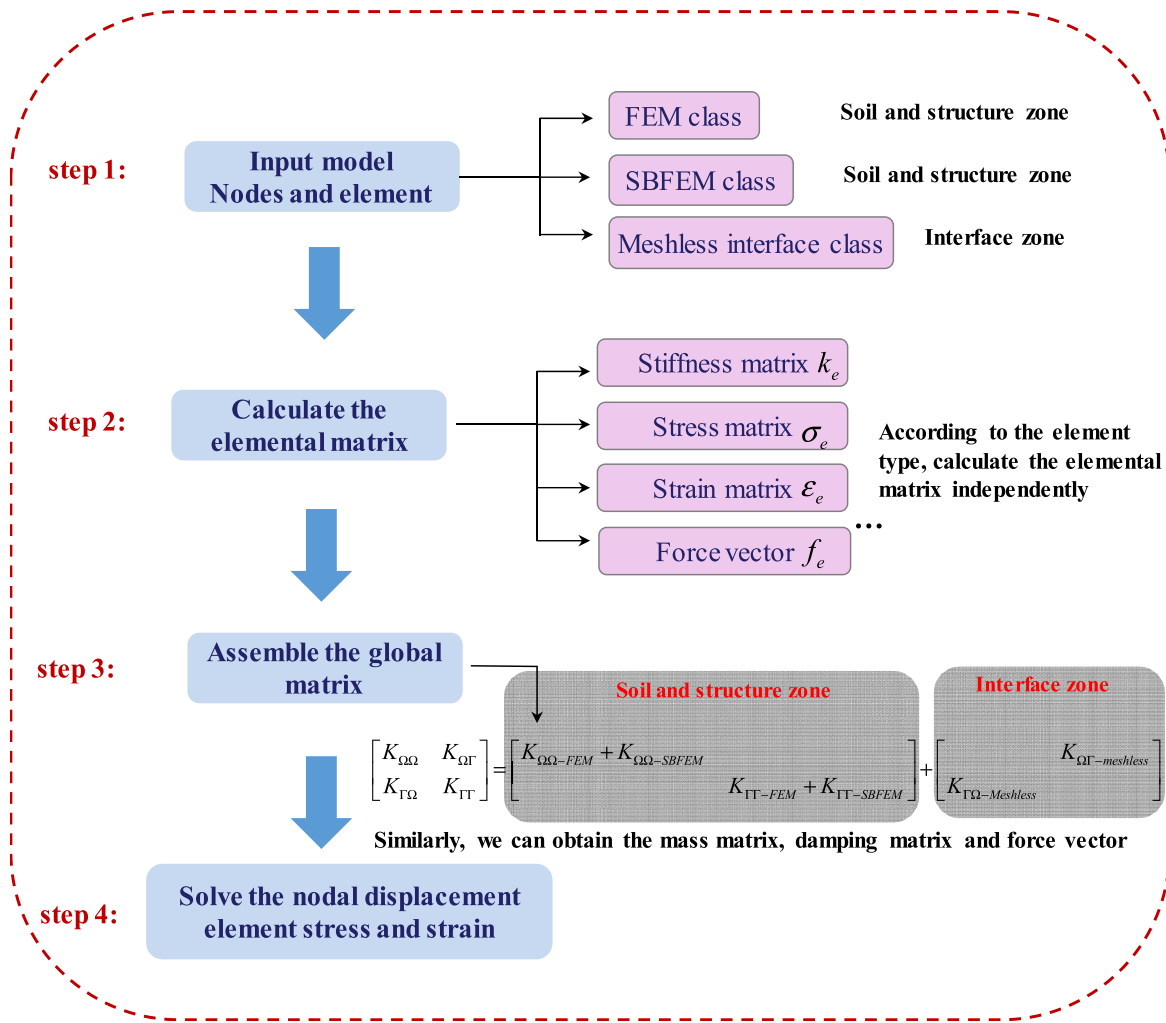


Fig. 7. The diagram of the algorithm coupling process.

Additionally, in section 2.4, the numerical implementation of the coupled method within uniformed frame is provided for as an example for readers.

2.1. The derivation of formulas of coupled Meshless-SBFEM-FEM

In this section, the derivation of the coupled Meshless-SBFEM-FEM is described in detail. The equation of motion for the displacement in each time step can be expressed as:

$$\mathbf{M} \frac{d^2 \mathbf{u}}{dt^2} + \mathbf{C} \frac{d\mathbf{u}}{dt} + \mathbf{K} \mathbf{u} = \mathbf{F} \quad (1)$$

Where \mathbf{M} , \mathbf{C} and \mathbf{K} represents the global matrices of mass, damping and stiffness. \mathbf{F} denotes the vector of applied forces and vector \mathbf{u} represents the nodal displacement. In this paper, the time period T divided into n time steps with the constant duration $\Delta t = \frac{T}{n}$ and the Newmark - β integration is adopted.

$$\mathbf{M} \ddot{\mathbf{u}}_{n+1} + \mathbf{C} \dot{\mathbf{u}}_{n+1} + \mathbf{K} \mathbf{u}_{n+1} = \mathbf{F}_{n+1} \quad (2)$$

In the SSI problem, the vectors and matrices are composed of three parts (soil zone, structure zone and interface zone). Then the equation can be re-written as:

$$\begin{bmatrix} M_{\Omega\Omega} & M_{\Omega\Gamma} \\ M_{\Gamma\Omega} & M_{\Gamma\Gamma} \end{bmatrix} \ddot{\mathbf{u}} + \begin{bmatrix} C_{\Omega\Omega} & C_{\Omega\Gamma} \\ C_{\Gamma\Omega} & C_{\Gamma\Gamma} \end{bmatrix} \dot{\mathbf{u}} + \begin{bmatrix} K_{\Omega\Omega} & K_{\Omega\Gamma} \\ K_{\Gamma\Omega} & K_{\Gamma\Gamma} \end{bmatrix} \mathbf{u} = \begin{bmatrix} P_{\Omega\Omega} \\ P_{\Gamma\Gamma} \end{bmatrix} \quad (3)$$

Matrices with " $\Omega\Omega$ " represent nodes within in soil zone while

matrices with subscript " $\Gamma\Gamma$ " comprise nodes within the structural zone. The matrices relating to the interface zone between soil and structure in are marked with the subscripts " $\Omega\Gamma$ " and " $\Gamma\Omega$ ". In the coupled Meshless-SBFEM-FEM approach, the soil zone and structural zones are simulated with FEM and SBFEM. However, the interface zone is simulated with the enhanced meshless interface. Then the above matrices and vectors can be expressed by equations (4)–(7):

$$\begin{bmatrix} M_{\Omega\Omega} & M_{\Omega\Gamma} \\ M_{\Gamma\Omega} & M_{\Gamma\Gamma} \end{bmatrix} = \begin{bmatrix} M_{\Omega\Omega-FEM} + M_{\Omega\Omega-SBFEM} & M_{\Gamma\Gamma-FEM} + M_{\Gamma\Gamma-SBFEM} \\ M_{\Omega\Gamma-meshless} \end{bmatrix} \quad (4)$$

$$\begin{bmatrix} C_{\Omega\Omega} & C_{\Omega\Gamma} \\ C_{\Gamma\Omega} & C_{\Gamma\Gamma} \end{bmatrix} = \begin{bmatrix} C_{\Omega\Omega-FEM} + C_{\Omega\Omega-SBFEM} & C_{\Gamma\Gamma-FEM} + C_{\Gamma\Gamma-SBFEM} \\ C_{\Gamma\Omega-Meshless} \end{bmatrix} \quad (5)$$

$$\begin{bmatrix} K_{\Omega\Omega} & K_{\Omega\Gamma} \\ K_{\Gamma\Omega} & K_{\Gamma\Gamma} \end{bmatrix} = \begin{bmatrix} K_{\Omega\Omega-FEM} + K_{\Omega\Omega-SBFEM} & K_{\Gamma\Gamma-FEM} + K_{\Gamma\Gamma-SBFEM} \\ K_{\Omega\Gamma-meshless} \end{bmatrix} \quad (6)$$

$$\begin{bmatrix} P_{\Omega\Omega} \\ P_{\Gamma\Gamma} \end{bmatrix} = \begin{bmatrix} P_{\Omega\Omega-FEM} + P_{\Omega\Omega-SBFEM} \\ P_{\Gamma\Gamma-FEM} + P_{\Gamma\Gamma-SBFEM} \end{bmatrix} \quad (7)$$

The subscripts "FEM", "SBFEM", "Meshless" denote the matrices and

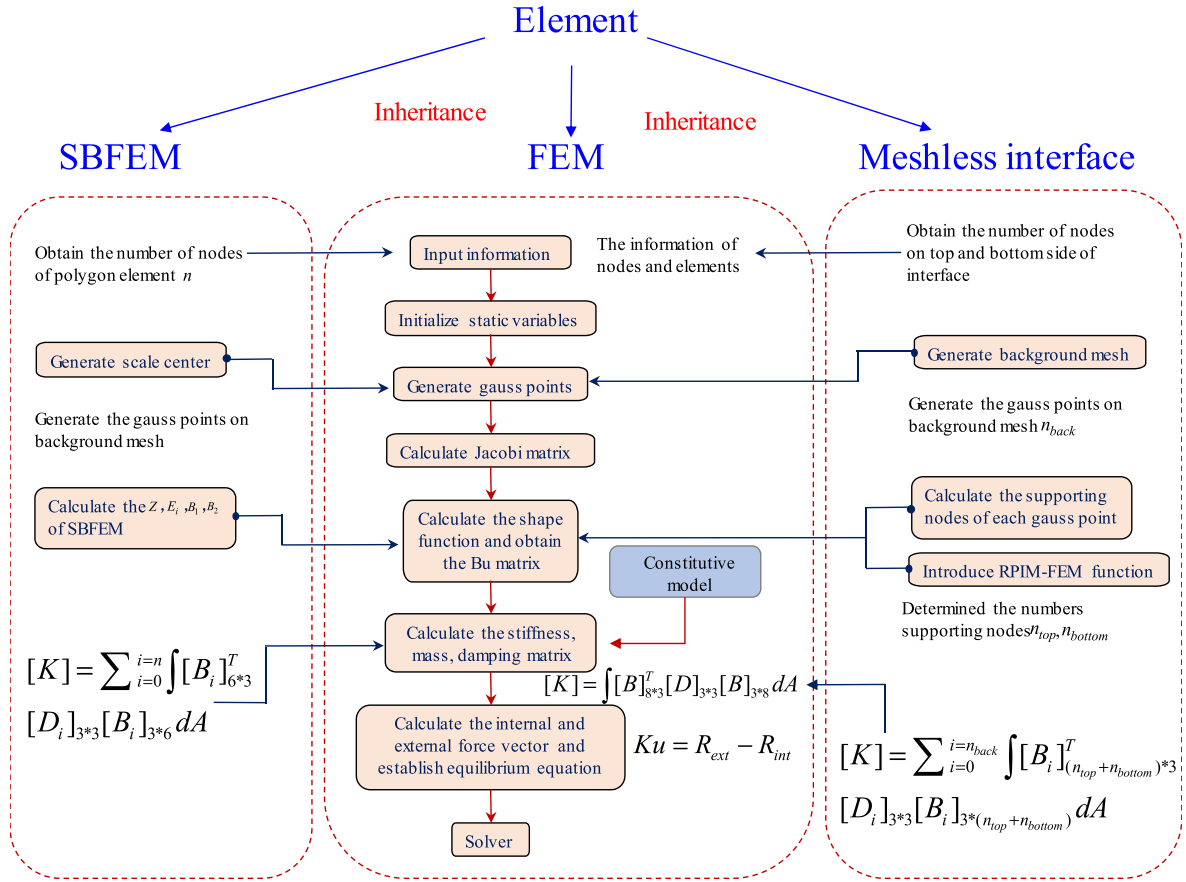


Fig. 8. Unified framework of the Meshless-SBFEM-FEM.

vectors computed by each method, respectively. The computation of each matrix and vector with each method (FEM, SBFEM, Meshless interface) is described in the following section.

2.2. The enhanced meshless interface

The above enhanced meshless interface is improved primarily in two aspects. Firstly, the precision near the boundaries of interfaces is improved through adding virtual nodes near the interface boundaries and introducing a modified RPIM function. Secondly, the meshless interface is extended towards being able to simulate circular (cambered) type interfaces by introducing circular type background mesh lines,

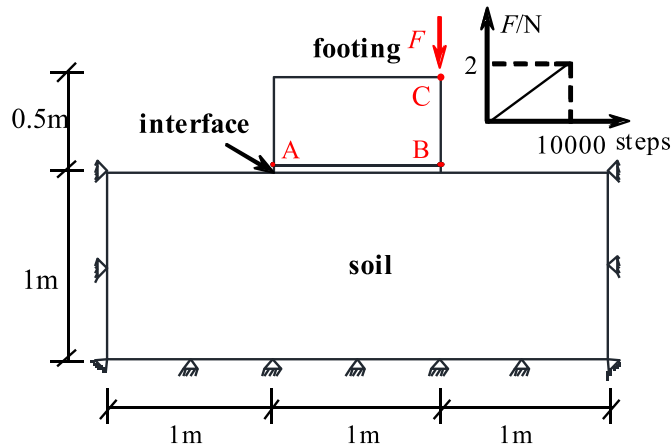


Fig. 9. The geometry of the footing-soil interaction model.

modifying the searching method for supporting nodes, and computing the shape functions. These two aspects are further detailed in sections 2.2.1 and 2.2.2, respectively. In addition, the computation of element matrices and vectors with the enhanced meshless interface is presented in section 2.2.3.

2.2.1. The improvement of accuracy near boundaries using modified RPIM interpolation

RPIM yields high accuracy within the solution domain, but suffers from a significant reduction of precision near boundaries as the number of supporting nodes of gauss points is decreased. Several papers [28,32] also mention this phenomenon, but do not give the solution. In this section, through introducing virtual nodes and combining the RPIM with linear interpolation function used in FEM, a modified interpolation function is introduced. Compared with the FEM linear interpolation function, the RPIM interpolation function is more accurate within the solution domain as enough supporting nodes of interpolation point are available [28]. However, when near the boundary of the solution domain, the number of supporting nodes reduces significantly, thus the precision is consequently decreased. We aim at combining the advantages of the above two interpolation functions and develop a modified RPIM function. Fig. 1 depicts the procedure for modified RPIM interpolation, and Fig. 2 shows the shape function of modified RPIM interpolation. In particular, the steps for above interpolation are as follows:

Table 1
Material parameters used in the simulation.

Footing		Soil		Interface	
E	ν	E	ν	K_s	K_n
$1.0 \cdot 10^6$	0.3	$1.0 \cdot 10^4$	0.3	$1.0 \cdot 10^4$	$1.0 \cdot 10^5$

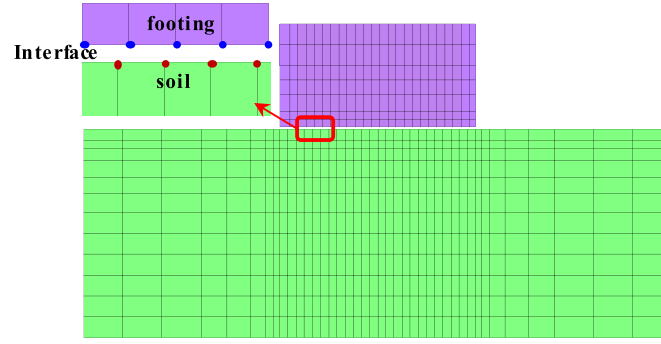


Fig. 10. The meshes of footing-soil interaction model.

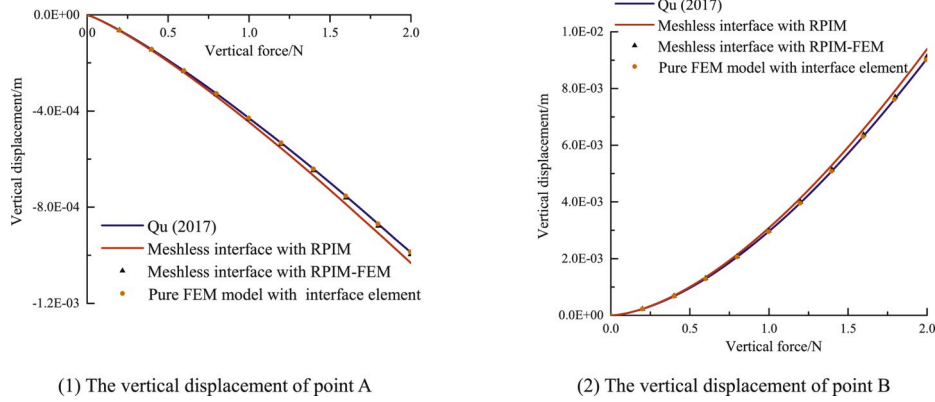


Fig. 11. The comparison of results with RPIM and modified RPIM.

Table 2

The absolute and relative error with RPIM and modified RPIM (vertical displacement of point A).

	0.5 N		1 N		1.5 N		2 N	
	Absolute error(mm)	Relative error	Absolute error(mm)	Relative error	Absolute error	Relative error	Absolute error	Relative error
RPIM	$2.4 \bullet 10^{-2}$	3.56%	$1.3 \bullet 10^{-1}$	3.98%	$2.2 \bullet 10^{-1}$	3.51%	$3.5 \bullet 10^{-1}$	3.82%
Modified RPIM	$5.0 \bullet 10^{-3}$	0.74%	$2.8 \bullet 10^{-2}$	0.87%	$4.5 \bullet 10^{-2}$	0.72%	$7.6 \bullet 10^{-2}$	0.83%

Table 3

The absolute and relative error with RPIM and modified RPIM (vertical displacement of point B).

	0.5 N		1 N		1.5 N		2 N	
	Absolute error(mm)	Relative error	Absolute error(mm)	Relative error	Absolute error	Relative error	Absolute error	Relative error
RPIM	$5.5 \bullet 10^{-3}$	4.72%	$1.7 \bullet 10^{-2}$	4.89%	$3.1 \bullet 10^{-2}$	4.71%	$4.8 \bullet 10^{-2}$	4.65%
Modified RPIM	$1.1 \bullet 10^{-3}$	0.91%	$3.1 \bullet 10^{-3}$	0.95%	$5.7 \bullet 10^{-3}$	0.84%	$8.8 \bullet 10^{-3}$	0.95%

- (1) Set virtual nodes near each side of the boundary.
- (2) Calculate the interpolated value of virtual nodes through the RPIM
- (3) function and the original nodes as follows,

$$u'(x) = \varphi_1(x)u_1 + \varphi_2(x)u_2 \dots + \varphi_n(x)u_n \quad (8)$$

where n represents the number of supporting nodes near the virtual point, $u'(x)$ refers to interpolated value of the virtual nodes, $u_n(x)$ refers to the value of each original node, and $\varphi_n(x)$ refers to the value of the RPIM interpolation function at each node.

- (3) Determine the position of the interpolated node. If the interpolated node is not near the boundary, then compute the value through RPIM with the original nodes. Further details for this step can be found in Ref. [29].

- (4) If the interpolated nodes are near the boundary, then compute their values through FEM linear interpolation over virtual nodes and boundary nodes (or the nodes closest to the boundary nodes) as follows,

$$u(x) = \left(\frac{a}{L}\right)u_1 + \left(1 - \frac{a}{L}\right)u'(x) = \left(\frac{a}{L}\right)u_1 + \left(1 - \frac{a}{L}\right)(\varphi_1(x)u_1 + \varphi_2(x)u_2 \dots + \varphi_n(x)u_n) \quad (9)$$

where $u(x)$ represents the value of interpolated point, a refers to the distance between the boundary node and the interpolated point, and L refers to the distance between the boundary node and the virtual node as shown in Fig. 1. Finally, replace the value of the virtual node with the result yielded from equation (8).

The interpolation function generally needs to satisfy certain important characteristics.

Table 4

The comparison of compute time (FE model vs enhanced meshless interface).

	The number of element	Compute time (s)	Normalized time
4-node interface element	813	953	1
Enhanced meshless interface	806	948	0.99

(1) Delta function

$$\varphi_i(x=x_i) = \begin{cases} 1, & i=j, j=1, 2, \dots, n \\ 0, & i \neq j, j=1, 2, \dots, n \end{cases} \quad (10)$$

As described in Equation (10), the i th shape function has zero values at all nodes except the i th node. Thus, the modified RPIM interpolation shows the delta function property (Fig. 2).

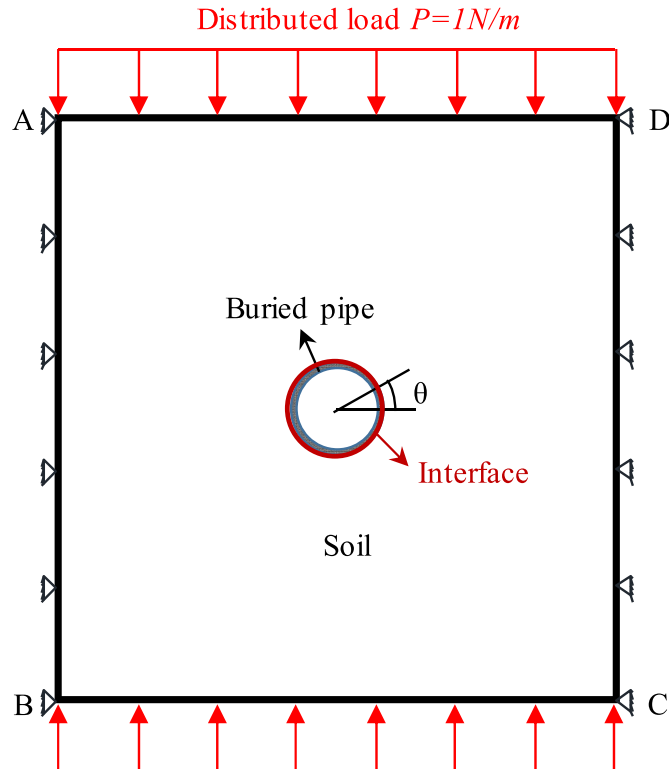
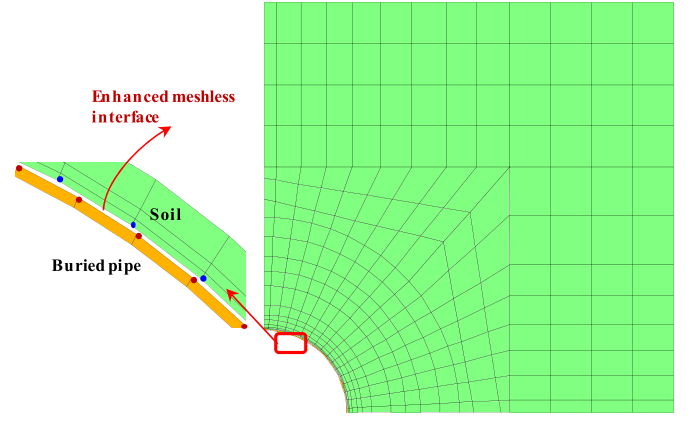
(2) Unity partition

$$\sum_{i=1}^n F_i(x) = 1 \quad (11)$$

This property ensures that rigid motion can be represented with the shape function. If the interpolated point is within the domain, this property can be fulfilled since the RPIM function possesses the properties of a unity partition. However, if the interpolated point is near the boundary, equation (12) can also be satisfied as follows

$$u(x) = f(x_1)u_1 + f(x')u'(x) \quad (12)$$

According to the properties of FEM and equation (9), $f(x_1) + f(x') = 1$. The value of the virtual node can be substituted by the results of equation (8). According to the property of the RPIM in equation (13). Finally, we can obtain the following equation and verify that the modified RPIM function indeed possesses the properties of the unity partition. It should be noted that $f_i(x)$ does not need to be located within

**Fig. 12.** The geometry of buried pipe model.**Fig. 13.** The meshes of the buried pipe model.

[0, 1].

$$\sum_{i=1}^n f_i(x) = 1 \quad (13)$$

$$u(x) = [f(x_1) + f(x')\varphi_1(x)]u_1 + f(x')\varphi_2(x)u_2 + \dots + f(x')\varphi_n(x)u_n \quad (14)$$

(3) Reproduction of linear basis

$$\sum_{i=1}^n x_i F_i(x) = x \quad (15)$$

Since the RPIM adds the basis $[1, x]$, RPIM can reproduce the linear basis. Thus, the interpolated point within the domain can satisfy this property. As FEM conducts linear interpolation, equation (16) can be obtained. Similarly, by substituting the value x of the virtual node according to equation (15), equation (17) can be obtained, which proves that the modified RPIM function can reproduce the linear basis.

$$x = f(x_1)x_1 + f(x')x' \quad (16)$$

$$x = [f(x_1) + f(x')\varphi(x_1)]x_1 + f(x')\varphi(x_2)x_2 + \dots + f(x')\varphi(x_n)x_n \quad (17)$$

(4) The continuity of shape function

The shape functions of RPIM and FEM are both continuous, thus the modified RPIM function is also continuous. The continuity of the shape functions can be visualized in Fig. 2.

The curve fits performed for RPIM and modified RPIM interpolation functions are estimated through one-dimensional functions. It should be noted that the linear basis is added to both interpolation functions mentioned above. The functions $y = 2x-1$ and $y = \sin \pi x$ are used as example functions to help verify the accuracy in curve fitting. Both functions are tested in the domain $[-2, 2]$ and the curve fitting of the functions using RPIM and modified RPIM is conducted through the following steps:

- (1) Select a set of nodes x_i within $[-2, 2]$ and compute the true value $f(x_i)$.
- (2) Choose a set of interpolated points x_j , and similarly obtain the corresponding true value.

Table 5

Material parameters used in buried pipe model.

Buried pipe		Soil		Interface			
E	ν	E	ν	K_{d0}	K_{n0}	c	R_z
$1.52 \cdot 10^{10}$	0.333	$2.067 \cdot 10^7$	0.25	$5.2 \cdot 10^7$	$1.7 \cdot 10^8$	0	0.98

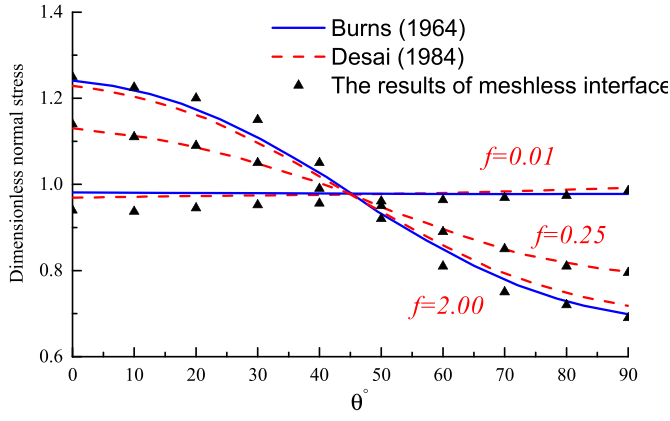


Fig. 14. Comparison of normal stresses along the interface.

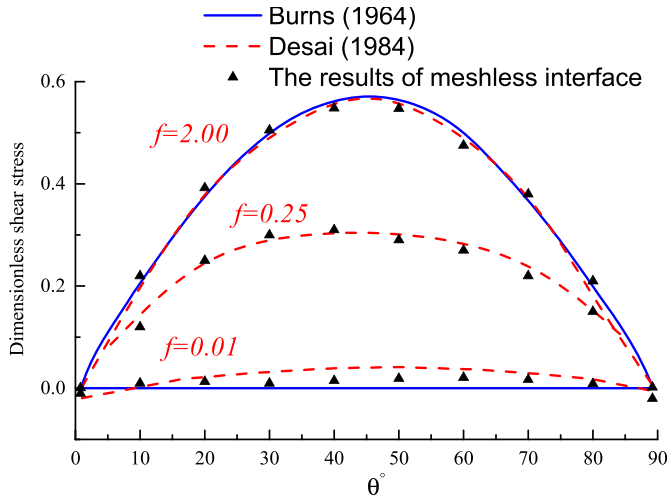


Fig. 15. Comparison of shear stresses along the interface.

- (3) Obtain the value of each interpolated point through RPIM and modified RPIM function.
- (4) Compute the error at each interpolated point using both interpolation functions and plot the fitted curves as shown in Fig. 3.

As both the interpolation functions use a linear basis and possess the properties of linearity, thus they can both reproduce linear functions. From the above results, we conclude that the RPIM shows adequate accuracy in fitting trigonometric functions, albeit with a significant drop of accuracy at the boundaries. On the other hand, the modified RPIM improves the accuracy at the boundaries and while maintaining high accuracy within the domain.

2.2.2. Theoretical derivation of circular (cambered) type's meshless interfaces

The existing meshless interface [31] can only simulate linear or

polyline types of soil-structure interaction. Since in practical geotechnical engineering, one can be faced with many circular (cambered) types of interfaces, including buried pipes, shield tunnels and three-arch type metro structures, etc., it is beneficial to extend the method to circular (cambered) type interfaces. The enhanced meshless interface provides three main modification as follows:

- (1) A circular (cambered) background mesh line is introduced for generation and integration of gauss points. Through coordinate transformations, the circular (cambered) background mesh line can be transformed into a line segments that can be expressed in linear, local coordinates shown in Fig. 4. Meanwhile, gauss points are generated on the line segment in local coordinates. After the gauss points are generated, the coordinate of gauss points are transformed back into global coordinates (the background mesh line for the circular type interface). The relevant formulations are as follows,

$$N_1 = \frac{1}{2}(1 - \zeta) \quad N_2 = \frac{1}{2}(1 + \zeta) \quad (18)$$

$$x = r \cos\left(\sum_{i=1}^2 N_i \theta_i\right) + x_0 \quad y = r \sin\left(\sum_{i=1}^2 N_i \theta_i\right) + y_0 \quad (19)$$

where r refers to the radius of the background mesh line, and (x_0, y_0) refer to the global coordinates of the center point.

Calculate the radius of the arc formed by each gauss point and its closest node by

$$\theta_{\min}(i) = \{\theta_{i,1} \dots \theta_{i,i-1} \theta_{i,i+1} \dots \theta_{i,n}\}_{\min} \quad (20)$$

in which

$$\theta_{i,j} = \arccos\left(\frac{(x_i - x_0, y_i - y_0) \times (x_j - x_0, y_j - y_0)}{r^2}\right) \quad (21)$$

Finally, if the node meets the following criteria, we can consider the node as part of the set of supporting nodes for the corresponding gauss point. In other words,

$$\|\theta_{i, \text{gauss}}\| \leq \text{alfs} \times \theta_{\min}(i) \quad (22)$$

where alfs refers to size of the influence domain, and according to reference [28] alfs equals 3. The variable $\theta_{i, \text{gauss}}$ refers to the angle of the arc formed by nodes and corresponding gauss point.

- (3) The basis added by the RPIM interpolation function is improved. The linear basis added by RPIM allows the shape function to maintain the advantages of polynomial interpolation and achieve stability [28]. In traditional meshless interfaces the added basis consists of constants and nodal coordinates $[1, x]$; however, in the enhanced meshless interface the basis is replaced by arc angles formed by nodes and the horizontal line $[1, \theta]$. The related formulas are discussed in the following, with further details found in Ref. [28].

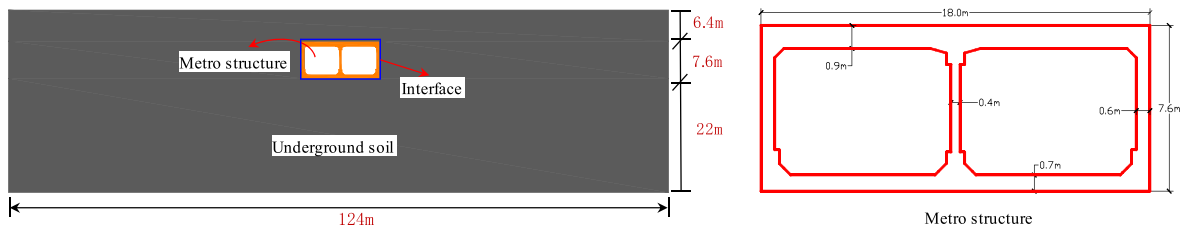


Fig. 16. The geometry of frame metro structure and underground soil model.

Mesh independently with FEM

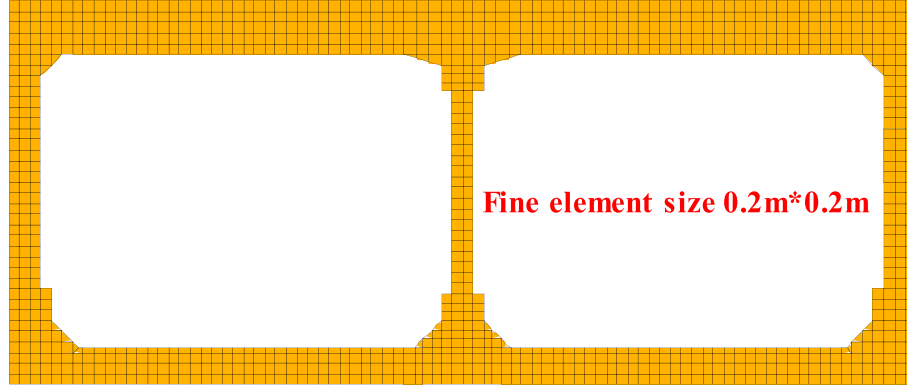


Fig. 17. The mesh of frame metro with FEM.

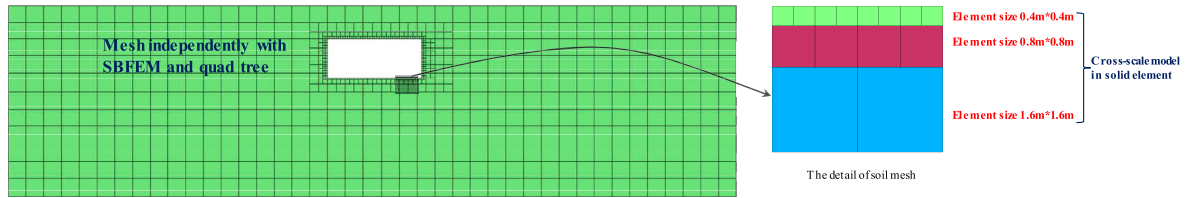


Fig. 18. The cross-scale mesh of soil generated using quad tree.

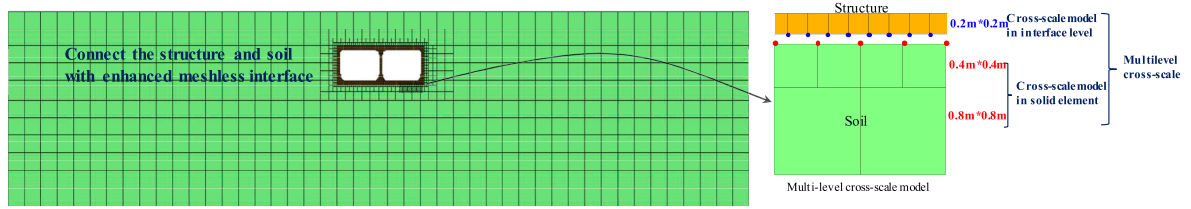


Fig. 19. The global cross-scale model of frame metro structure.

The displacement along the each surfaces of interface can be described with RPIM functions,

$$u = \sum_{i=1}^n B_i(r) a_i + \sum_{j=1}^2 P_j(\theta) b_j \quad (23)$$

where

$$B_i(r) = (r_i^2 + C^2)^q \quad (24)$$

In equation (23) n refers to the number of supporting nodes for each gauss point, B_i represents the multi-quadric radial basis, and P_j represents the added basis. Furthermore, a_i and b_j are constants, which can be obtained by

$$\begin{bmatrix} u \\ 0 \end{bmatrix} = \begin{bmatrix} R & P \\ P^T & 0 \end{bmatrix} \begin{bmatrix} A \\ B \end{bmatrix} \quad (25)$$

where

$$[AB]^T = [a_1 a_2 \dots a_n b_1 b_2] \quad (26)$$

In equation (25)

$$R = \begin{bmatrix} B_1(r_1) & B_2(r_1) & \dots & B_n(r_1) \\ B_1(r_2) & B_2(r_2) & \dots & B_n(r_2) \\ \dots & \dots & \dots & \dots \\ B_1(r_n) & B_2(r_n) & \dots & B_n(r_n) \end{bmatrix} \quad (27)$$

$$P^T = \begin{bmatrix} 1 & 1 & \dots & 1 \\ \theta_1 & \theta_2 & \dots & \theta_n \end{bmatrix} \quad (28)$$

In equations (27) and (28), r_i refers to the relative distance between nodes and gauss points, θ_i refers to the arc angle formed by nodes and the horizontal line. Finally, the a_i and b_j can be obtained as follows

$$a = S_a u_e = R^{-1} [1 - P S_b] u_e \quad (29)$$

$$b = S_b u_e = [P^T R^{-1} P]^{-1} P^T R^{-1} u_e \quad (30)$$

2.2.3. Computation of element matrices with the enhanced meshless interface

In this section, the computation of meshless interface element matrices and vectors are presented. The displacement can be re-written as

$$u(x) = [R^T(x) S_a + P^T(x) S_b] = \Phi(\mathbf{x}) u_e = \{\varphi_1 \varphi_2 \dots \varphi_n\} u_e \quad (31)$$

Table 6
Material parameters of metro structure in concrete plastic damage model.

Metro structure						
$\rho/\text{kg/m}^3$	E/GPa	ν	f_t/MPa	f_c/MPa	l_c/m	$G_t/\text{N}\cdot\text{m}^{-1}$
2450	31	0.167	3.48	27.6	0.4	325

Table 7
Material parameters of underground soil in generalized plastic interface model.

Interface															
Elastic modulus		Critical state			Particle breakage			Plastic direction		Loading direction		Plastic modulus			
D_{s0}/kPa	D_{n0}/kPa	M_c	e_{r0}	λ	$a/\text{kPa}^{0.5}$	b	c	α	r_d	k_m	M_f	k	H_0/kPa	f_h	
1000	1500	0.88	0.4	0.091	5000	1.38	0.1	0.65	0.2	0.6	0.65	0.5	8500	2	

where ϕ_i is the shape function at node i . The relative displacement of each gauss point within the interface zone can be obtained as follows (taking the x direction for example)

$$\Delta_u = \{\varphi_1 \varphi_2 \dots \varphi_{n_{top}}\} \begin{Bmatrix} u_1 \\ u_2 \\ \dots \\ u_{n_{top}} \end{Bmatrix} - \{\varphi_1 \varphi_2 \dots \varphi_{n_{bottom}}\} \begin{Bmatrix} u_1 \\ u_2 \\ \dots \\ u_{n_{bottom}} \end{Bmatrix} \quad (32)$$

where n_{top} , n_{bottom} represent the surrounding nodes of each gauss point along the top or bottom surfaces, respectively. Then, the matrix expressing the differential movements of each gauss point can be describe by

$$B_i = \begin{bmatrix} \varphi_1 & 0 & \varphi_2 & \dots & \varphi_{n_{top}} & 0 & -\varphi_1 & 0 & \dots & -\varphi_{n_{bottom}} & 0 \\ 0 & \varphi_1 & 0 & \varphi_2 & \dots & \varphi_{n_{top}} & 0 & -\varphi_1 & \dots & 0 & -\varphi_{n_{bottom}} \end{bmatrix} \quad (33)$$

Through integration within the background mesh line, the stiffness matrix of meshless interface within each background mesh can be denoted by:

$$K^e = \sum_{i=1}^n \int_{-\frac{l}{2}}^{\frac{l}{2}} B_i^T D_i^e B_i dx \quad (34)$$

where n presents the gauss number in each background mesh, l denotes the length of the background mesh line and $[D_i]$ is the constitutive model matrix employed in the interface zone. Meanwhile, the internal force vector can be solved by equation (35),

$$P_{int}^e = \sum_{i=1}^n \int_{-\frac{l}{2}}^{\frac{l}{2}} B_i^T \sigma_i dx = \sum_{i=1}^n \int_{-\frac{l}{2}}^{\frac{l}{2}} B_i^T D_i^e B_i u dx \quad (35)$$

where u represents nodal displacement. The mass matrix can be ignored within the interface zone. The damping matrix can be computed through the Rayleigh damping [44] (the parameters can be found in section 3.3). More details can be found in Ref. [31].

2.3. The scale boundary finite element method (SBFEM)

In the 1990s, Wolf and Song [33,34] developed the SBFEM, which combines the advantages of FEM and boundary element method (BEM). By setting a scaling center and dispersing the boundaries, one can obtain

Table 8
Material parameters of underground soil in generalized plasticity model.

Underground soil																
Elastic modulus				Plastic loading direction				Plastic modulus								
G_0	K_0	m_s	m_v	M_g	M_f	α_f	α_g	m_l	m_u	r_d	γ_{DM}	γ_u	β_0	β_1	H_0	H_{U0}
800	1000	0.4	0.4	1.38	0.45	0.25	0.40	0.14	0.5	20	70	5	25	0.01	2450	1600

an analytical solution in the radial direction and a numerical solution in the circumferential direction. Through the introduction of internal gauss points, Chen et al. extended the SBFEM to nonlinear analyses shown in Fig. 6. The coupled SBFEM-FEM can work together with quad-tree technique [10] and achieve cross-scale model in solid elements.

Since the previous processes, including coordinate transformation, calculate the shape function and strain matrix are consistent with the SBFEM provided by Song, the corresponding formulas are not given in detail. The shape function can be obtained through the gauss points at the boundary and can be expressed by equation (36).

$$\varphi(\xi, s) = N_u(s) \psi \xi^{-S_n} \psi^{-1} \quad (36)$$

The strain matrix can be expressed as follows

$$B_i = [B_1(s) \psi_u [-S_n] + B_2(s) \psi_u] \xi^{-S_n - I} \psi_u^{-1} \quad (37)$$

where s denotes the circumferential coordinate, ξ denotes the radial coordinate and more details can be found in Refs. [33,34]. Then, unlike traditional SBFEM, the stiffness matrix is computed by the integration of internal gauss points as shown in equation (38),

$$K^e = \sum_{i=1}^m B_i^T D_i^e B_i A_i \quad (38)$$

where m presents the internal gauss number in each SBFEM element. Similarly, the mass matrix can be computed by

$$M^e = \sum_{i=1}^m \rho_i \varphi_i^T \phi_i A_i \quad (39)$$

The damping matrix can be computed through the Rayleigh damping (the parameters can be found in section 3.3).

$$[C]^e = \alpha [M]^e + \beta [K]^e \quad (40)$$

The internal force vector and external force vector can be obtained by

$$R_{int} = \sum_{i=1}^m B_i^T \sigma_i A_i = \sum_{i=1}^m B_i^T D_i^e B_i u A_i \quad (41)$$

$$R_{ext} = \int_{\Omega} \varphi_i^T f_b d\Omega \quad (42)$$

where f_b presents the body force. All the matrices and vectors used in SBFEM elements are shown above and more details can be found in Refs. [10].

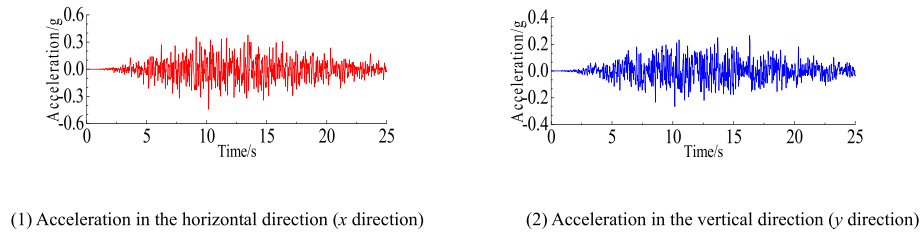


Fig. 20. Time history of the acceleration during earthquake.

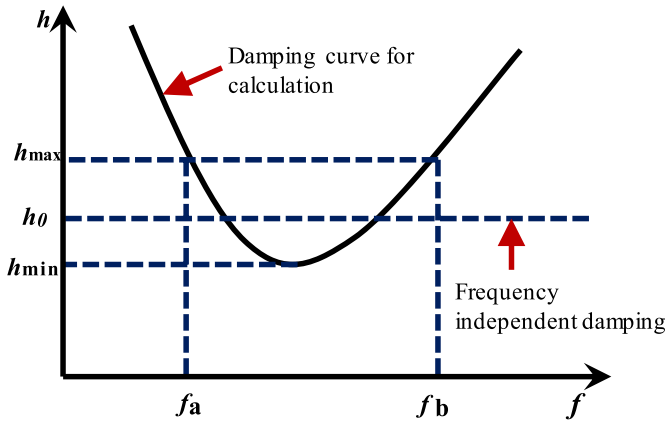


Fig. 21. The relation between damping ratio and frequency [45].

2.4. The numerical implementation of coupled meshless-SBFEM-FEM

In previous work, SBFEM-FEM [10,11,35] and the coupled FE model with meshless interface [31,36,37] were applied to solve SSI problems. However, the introduced Meshless-SBFEM-FEM in this paper is a more efficient and effective way to solve SSI problems by enabling multilevel cross-scale modeling, independent meshing and local mesh optimization. Though the coupled Meshless-SBFEM-FEM is an effective tool in solving SSI problems, there are currently no commercially available software that can enable the coupling of the above numerical algorithms. The custom developed software, while amenable to customized computational routines, lacks the powerful analysis capabilities of most FEM software (e.g. constitutive models, loading, solvers), and is time-consuming to use and develop. Thus, the best of both worlds can be achieved by integrating the SBFEM and meshless interfaces into the existing FEM software. In this paper, through the object-oriented C++ language, the SBFEM and meshless interface is integrated into the custom FEM software platform named GEODYNA.

The GEODYNA software platform is based on C++, object-oriented programming, parallel computing, and other advanced technologies to enable accurate analysis of models under static loading, consolidation, dynamic loading, liquefaction, stability, permanent deformation, etc.

Until now, GEODYNA has been successfully applied as an analysis tool for 59 projects included conservancy projects, nuclear power projects, marine traffic engineering and analysis of underground structures. In order to facilitate the understanding and usage of the introduced method, the implementation of the coupled Meshless-SBFEM-FEM method is shown in terms of a diagram in Fig. 7. The procedure can be summarized into four steps:

- (1) Input the model with information about the nodes and elements (need to distinguish the element types).
- (2) Compute the matrices within element. Each element type (FEM, SBFEM, Meshless interface) owns an independent process, including calculate the stiffness, mass, stress, strain matrices and force vector.
- (3) Assemble the global matrices according to the nodal ID.
- (4) Compute the nodal displacements, and the strains and stresses of each element.

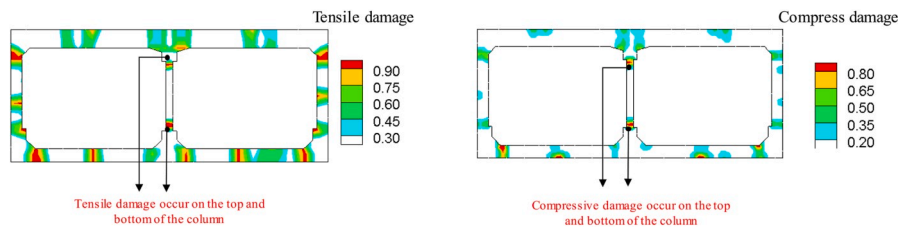
The core of the coupling method lies in step 2 (compute the elemental matrix). Thus, the implementation of each class (FEM, SBFEM, Meshless interface) are also presented in Fig. 8. Each class has its own characteristics and commonalities; thus we can set the shape function, gauss integration, forming stiffness, mass, damping matrix, etc. as public member functions. Conversely, the computational scale center, formation of the background mesh, and RPIM interpolation are set as private member functions of each class.

3. Numerical examples

3.1. Simulating footing-soil interaction

As mentioned in prior sections, the RPIM interpolation function used in meshless interfaces may cause errors near the boundary. However, the developed modified RPIM function can avoid this issue. Thus in this section the simulation of footing-soil interaction is presented to demonstrate the improved performance of the modified RPIM interpolation function near the boundary.

The soil model is 3 m long and 1 m wide with constraints at the side and bottom boundaries. A rectangle footing with 1 m length and 0.5 m width lies on top of the soil. To verify the behavior of the interface in the



(1) The distribution of tensile damage

(2) The distribution of compressive damage

Fig. 22. The damage distribution within the frame metro structure.

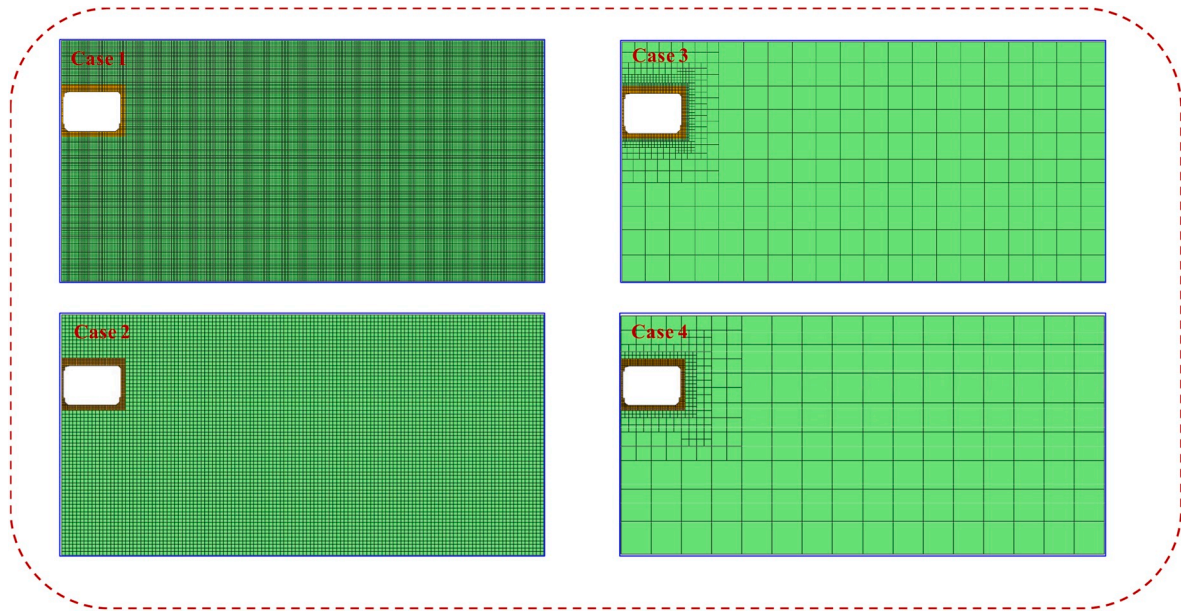


Fig. 23. The comparison of the meshes from the four models (1/2 sectioned view).

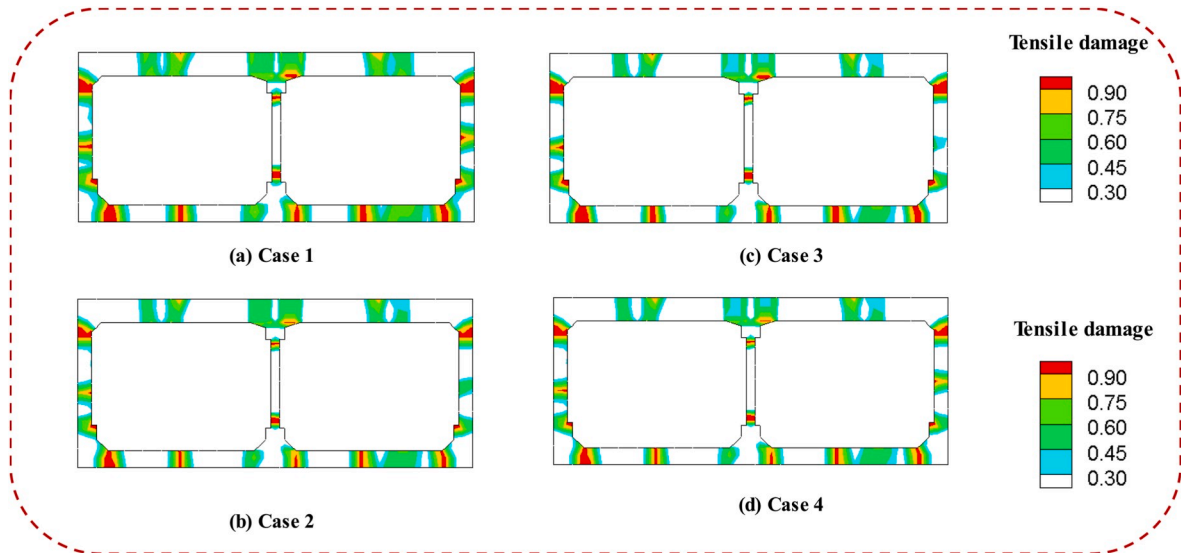


Fig. 24. The comparison of tensile damage of frame structure across the 4 models.

normal direction, a vertical load F is applied on point C (top right corner) with 0.002 N increments until 2.0 N is reached. The self-gravity is ignored. The geometry and boundary conditions used in the simulation are illustrated in Fig. 9. The soil, structure and interface all adopt the linear elastic model summarized in Table 1. Meanwhile, the interface is considered as having zero-thickness in the normal direction. As the enhanced meshless interface can connect soil and structure elements that have different sizes, thereby allowing the soil and the structure to be meshed independently as shown in Fig. 10.

Two cases are taken into consideration. In case 1 the interpolation function of the meshless interface uses RPIM while the modified RPIM interpolation function is used in case 2. In addition, the results of Qu (2017) [23] and the results with pure FE model are included for comparison. The displacements of point A and point B in both cases are shown in Fig. 11.

From the results we can conclude that the vertical displacements of points A and B obtained by the modified RPIM interpolation function matches well with the results obtained by Qu (2017) [23] and the FE

model. The results of the RPIM interpolation function show a consistent trend but gain absolute error as the force increases. However, the value of the relative error fluctuates within a range. The corresponding results are summarized in Tables 2 and 3 as follows.

A comparison of the computing time is shown in Table 4. The results demonstrate that the computational efficiency of meshless interface and FE model are almost the same (the number of element is nearly the same).

In the above example, the RPIM interpolation function decreases in accuracy near the boundary. However, the modified RPIM interpolation function avoids this issue. Thus, the meshless interface enhanced with a modified RPIM interpolation is effective and has great potential for use in practical geotechnical engineering.

3.2. Simulating a buried pipe

The traditional meshless interface [31] works only with linear or polyline types of soil-structure interaction. In this section, the enhanced

Table 9

The comparison of computing time across the 4 models.

	Model	Number of frame element	Number of frame element	Normalized time
Case 1	FEM	1022	82698	1
Case 2	FEM-Meshless	1022	14144	0.48
Case 3	FEM-SBFEM	1022	3948	0.35
Case 4	FEM-SBFEM-Meshless	1022	2364	0.24

Table 10

The detail of time consuming with FE model.

Main process	Calculating element matrices	Forming global matrices	Non-linear iteration	Calculating element vectors	Solver
Time consuming	4.2%	2%	28.1%	25%	40.7%

meshless interface is extended for simulating circular (cambered) type interfaces. Specifically, a simulation of a buried pipe is presented to verify that the enhanced meshless interface can be applied to simulate circular type interfaces. The buried pipe is a classic problem, and several authors have conducted research on this simulation [12,38]. In addition, Burns and Richards [39] has provided the analytic solution to this problem when the interface is completely adhesive ($f = 2.0$) and has complete adhesion smoothness ($f = 0$).

The radius R of the buried pipe is 0.84 m, and the pipe thickness is 0.1 m. The soil region is 4.2 m (AB)•4.2 m (BD). The interface between the soil and the structure is simulated with 3.3 mm in thickness direction. The uniformly distributed load $p = 1 \text{ N/m}^2$ is applied on the top and bottom surfaces of the soil. The detail of geometry and boundary conditions are shown in Fig. 12. Due to symmetry, only a quarter model is considered for calculation (Fig. 13). Both the pipe and soil are simulated with linear elastic models. The hyperbolic model of strain hardening (Clough and Duncan [14]) is adopted to model the interface behavior in the shear direction. The constitutive model is presented by the relevant equation.

$$K_s = K_{s0} \left(1 - \frac{R_r}{c - f\sigma_n} \right)^2 \quad (43)$$

where c is the cohesion, f is the friction coefficient, K_{s0} is the initial tangent stiffness and R_r is a constant less than 1.

In the normal direction, instead of a constant stiffness typically used by a Good-man interface element, the hyperbolic model by S. C. Bandis [40] is applied, as shown in equation (44),

$$K_n = \frac{K_{n0}}{\left(1 + \frac{v}{t} \right)^2} \quad (44)$$

where v is relative displacement in normal direction and t is the thickness of the interface, and k_{n0} is the initial normal stiffness. The material characteristics in this simulation are summarized in Table 5.

Three subcases are simulated corresponding to three different values for coefficient $f \{0.01, 0.25, 2\}$ [12,38]. The dimensionless normal stress and stress along the interface are shown in Fig. 14 and Fig. 15. The analytic solution given by Burns and Richards [39] is also included for comparison. The results of the simulation performed by Desai et al. [12]

with thin layer elements are also shown.

The results yielded by the enhanced meshless interface are consistent with the solution of [12,39] for the normal and shear stresses along interface. We can conclude that the enhanced meshless interface can be extended to circular (cambered) type interfaces.

3.3. Simulating a frame metro structure

As an essential transportation tool, the subway offers can greatly ease traffic congestion. A significant number of people has recently chosen subway as the preferred mode of transit. Thus, as a potential matter of

public safety, it is of great significance to capture the dynamic reaction of metro structure under earthquake excitation. In this section, the enhanced meshless interface coupled with SBFEM and FEM can achieve flexibility in cross-scale modeling and effectively capture the damage evolution of structure.

3.3.1. Cross-scale model

Fig. 16 depicts the geometry of model for the frame metro structure and underground soil. The soil is 124 m long and 36 m deep (included 6.4 m burial depth). To conduct fine analysis of the structure, the metro structure is independently meshed by with elements of size $0.2 \text{ m} \times 0.2 \text{ m}$ as shown in Fig. 17.

If the underground soil shares the same element size as the structure, the computation efficiency will be significantly decreased due to the necessary introduction of many elements. Thus, the SBFEM and quad tree technique are used to mesh the underground soil. Through three levels of the quad tree technique, the size of soil mesh increased from $0.4 \text{ m} \times 0.4 \text{ m}$ – $3.2 \text{ m} \times 3.2 \text{ m}$ (Fig. 18).

As the soil and structure are meshed independently, the nodes along the both sides of interface do not match. However, the enhanced meshless interface can directly connect the soil and structure by introducing flexible nodes. Thus, the enhanced meshless interface coupled with FEM-SBFEM achieves global cross-scale model from 0.2 m to 3.2 m element sizes. In addition, the enhanced meshless interface avoids the mutual interference between soil and structure meshes. The final model is shown in Fig. 19. The multilevel cross scale model uses only 3286 elements to conduct a detailed analysis of the frame metro structure.

3.3.2. Material parameters

To simulate the damage evolution of the structure, the generalized plasticity constitutive model [41] is applied to model the underground soil; meanwhile, the interface zone is simulated with a generalized plastic interface model [42] to capture the complex behaviors include crack opening, closure and sliding during the earthquake. Meanwhile, the plastic damage model [19,43] is introduced to simulate the dynamic response of the frame metro structure while considering the stiffness degeneration that occurs with damage. It should be noted that all the material parameters can apply to both static and dynamic damage analysis. The details of each component are summarized in Table 6 (metro structure), Table 7 (interface) and Table 8 (underground soil).

Table 11

The detail of time consuming with coupled Meshless-SBFEM-FEM model.

Main process	Calculating element matrices			Coupling global matrices			Non-linear iteration	Calculating element vectors			Solver
	FEM	SBFEM	Meshless	FEM	SBFEM	Meshless		FEM	SBFEM	Meshless	
Time consuming	1.1%	4.3%	3.9%	0.6%	2.7%	2.9%	21.2%	6.2%	13.3%	11.7%	32.1%

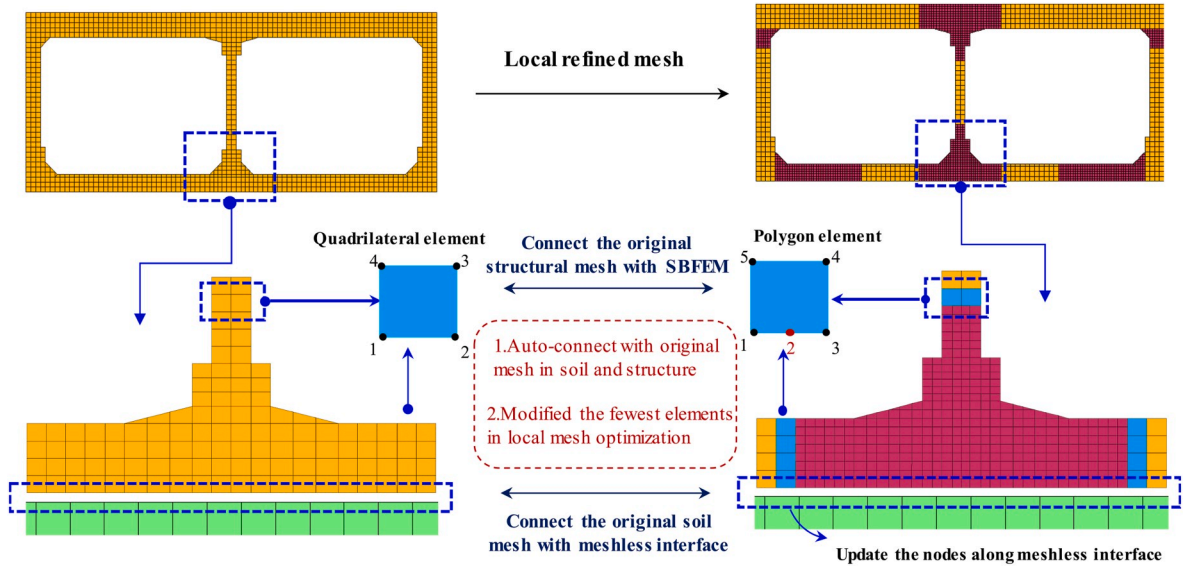


Fig. 25. Local mesh optimization with coupled Meshless-SBFEM-FEM.

3.3.3. Dynamic damage analysis

The input ground motion is a 25 s seismic wave with a peak acceleration 0.497g in the horizontal direction and 0.334g in the vertical direction (Fig. 20). The dynamic analysis method utilizes Newmark- β [44] integration with 0.01s in each calculation step as following:

$$\dot{u}_{t+\Delta t} = \dot{u}_t + [(1-\gamma)\dot{u}_t + \gamma\ddot{u}_{t+\Delta t}]\Delta t \quad (45)$$

$$u_{t+\Delta t} = u_t + \dot{u}\Delta t + \left[\left(-\frac{1}{2} - \alpha \right) \ddot{u}_t + \alpha \ddot{u}_{t+\Delta t} \right] \Delta t^2 \quad (46)$$

To guarantee the unconditional stability of solution and neglect the artificial numerical damping, the integral parameter $\gamma = 0.5$, $\alpha = 0.5$, integration step $\Delta t = 0.01$ s and the convergence precision is set as 5%.

The damping matrix $[C]$ is related to the viscous coefficient of the material. The Rayleigh damping [45] is often chosen to reflect the damping characteristics of soil. The damping matrix can be expressed as follows:

$$[C] = \alpha[M] + \beta[K] \quad (47)$$

where α and β are both damping coefficients. Yoshida et al. [45] proposed that the minimum damping ratio can be expressed as

$$h_{\min} = \sqrt{\alpha\beta} \quad (48)$$

Then, a sensitive frequency range f_a and f_b needs to be defined. In geotechnical engineering, this range is typically between 0.5 and 5 Hz. The damping ratio at the boundary of rate can be expressed as

$$w = 2\pi f \quad (49)$$

$$h_{\max} = \alpha/2w_b + \beta w_b/2 \quad (50)$$

$$h_{\max} = \alpha/2w_a + \beta w_a/2 \quad (51)$$

where the frequency-dependent damping can be expressed by:

$$h_0 = (h_{\min} + h_{\max})/2 \quad (52)$$

Through the above equation, the damping coefficients α and β can be calculated. When the damping ratio $h < h_0$, the following is set: $h = h_0$. The relation between damping ratio and frequency is shown in Fig. 21. In this paper, the $f_a = 0.5$, $f_b = 3$ and $h_0 = 0.2$.

The tensile damage and compressive damage of the metro structure obtained from dynamic damage analysis are shown in Fig. 22. From the results we can conclude that the tensile damage and compressive damage occur most severely at the top and bottom of the central column, which is consistent with the previous findings in literature and the actual damage [46,47].

To verify the high efficiency and flexibility of the coupled Meshless-SBFEM-FEM approach, three more models are considered as follows: Case 1: model with FEM; Case 2: model with FEM and meshless interfaces. Case 3: model with SBFEM-FEM. And for comparison, case 4 exhibits a model with the full Meshless-SBFEM-FEM combination. The models are shown in Fig. 23. To more clearly depict the model, only 1/2 of the model, which is symmetric, is presented. A comparison of the tensile damage results and computing time (dynamic analysis) are

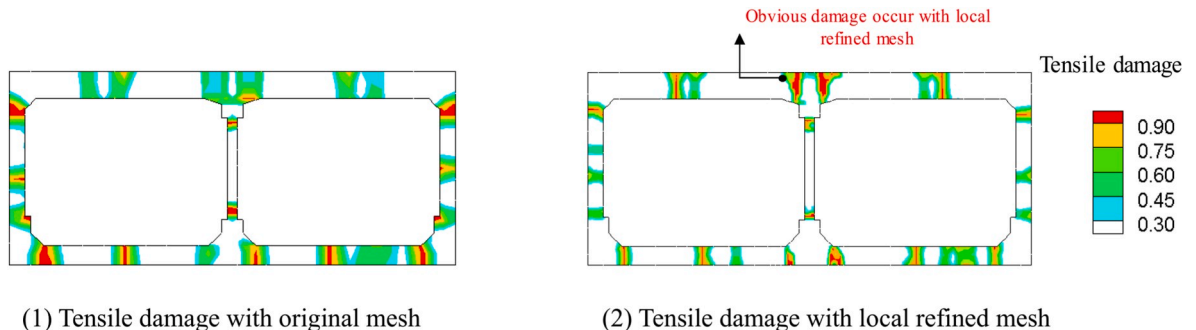


Fig. 26. Comparison of tensile damage (original mesh vs local refined mesh).

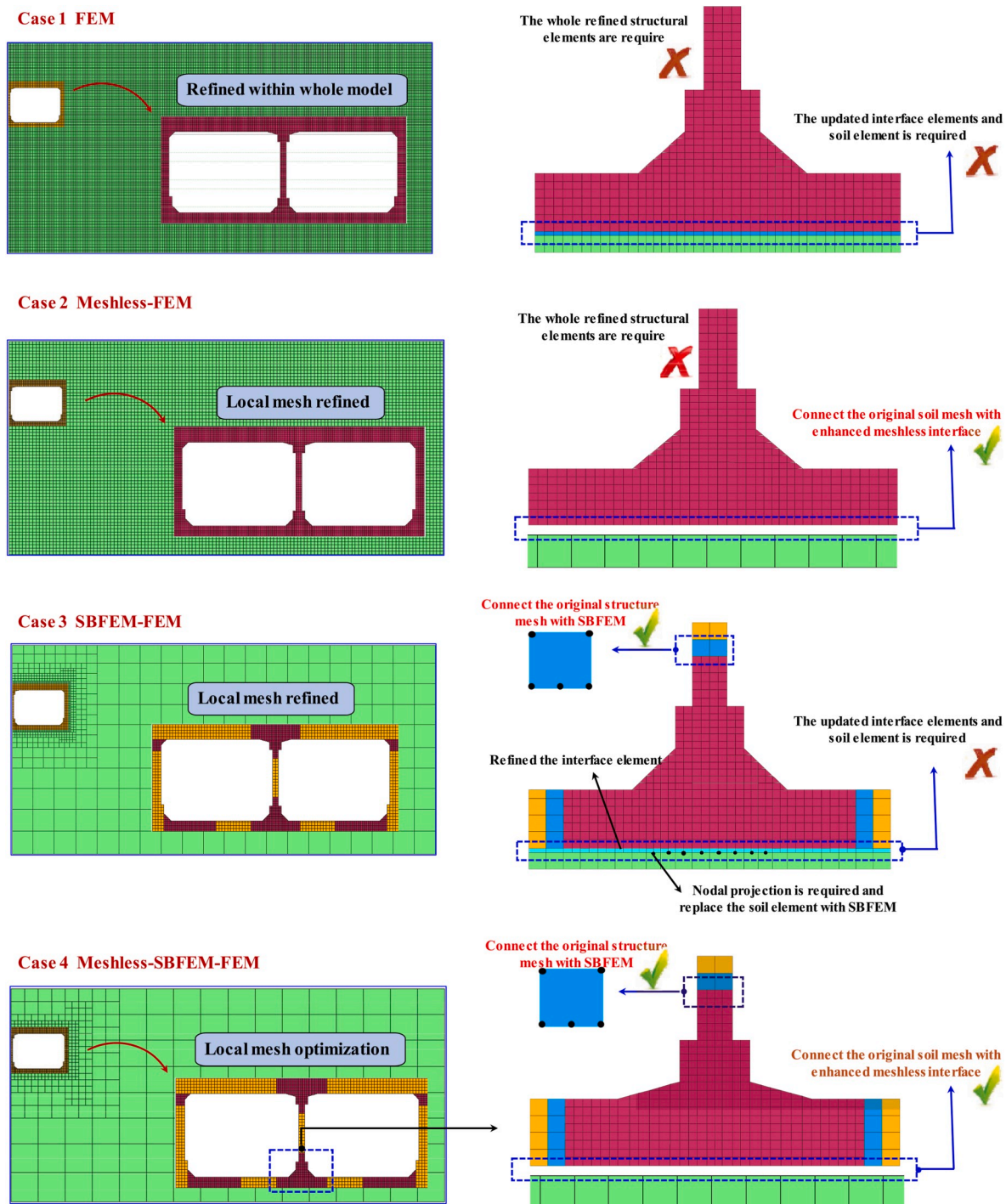


Fig. 27. Comparison of local mesh optimization between the 4 models.

Table 12
Comparison of computing time (FEM vs coupled Meshless-SBFEM-FEM).

Model	Original model		Refined model		Normalized time
	Structure mesh	Soil mesh	Structure mesh	Soil mesh	
FEM	1022	82698	2040	326892	1
FEM-SBFEM-Meshless	1022	2264	1148	2264	0.11

shown in Fig. 24 and Table 9.

The results show that the cross-scale model (case 2–4) can reflect the distribution of high tensile damage zone computed by refined pure FE model. From the results, we can conclude that the coupled Meshless-SBFEM-FEM can significantly reduce the number of elements and improve the computational efficiency compared to the scenario where only a traditional FEM model and single cross – scale method (case 2 and case 3) are utilized. In addition, the divided calculation times of coupled Meshless-SBFEM-FEM and pure FE model according to main process and each algorithms are summarized in Tables 10 and 11.

Due to the complexity of the meshless method and SBFEM in forming the shape function, it takes more time for SBFEM to compute element matrices and vectors compared to the pure FE model. In addition, more nodes are needed in each meshless interface and SBFEM element, thus increasing the time consumed in coupling global matrices. However, the number of degrees of freedom (DOFs) within the whole model is reduced through the SBFEM and meshless method, and thus the coupled Meshless-SBFEM-FEM approach saves much time during non-linear iterations and the solving process.

3.3.4. Local mesh optimization

Results from previous literature show that a refined mesh can yield more precise and accurate predictions about the damage zones [19]. To obtain a detailed distribution of damage in the metro structure, the meshes of the model needs to be refined. In this example, through the SBFEM and enhanced meshless interface, only the mesh in high damage zone needs to be replaced. The replacement process is as follows: (1) Delete the elements and nodes in high damage zones. (2) Generate the refined mesh in the damage zones. (3) Through adding the hanging nodes, the FEM elements connected to the high damage zone can be changed into SBFEM elements. (4) Adjust the nodes on the surface of the enhanced meshless interface and re-connect with the original soil mesh. The final mesh is shown in Fig. 25.

A comparison of the tensile damage sustained by the metro structure with original meshes vs the local refined meshes are shown in Fig. 26. The distribution of damage region shows more details and shows that the top of structure suffered from more significant damage. From the results, we can conclude that refined meshes are necessary for fine dynamic damage analysis of such metro structures.

Without coupled Meshless-SBFEM-FEM, local mesh optimization can be a time consuming and complex process, as shown in Fig. 27. A

comparison of the number of elements and computation time is listed in Table 12 (FEM vs Meshless-SBFEM-FEM). The results demonstrate that the introduced method simplifies the process of local mesh optimization, increases the utilization of original mesh and decreases computation time.

From this example, we demonstrate that the enhanced meshless interface coupled with FEM-SBFEM can allow independent meshing of adjacent model parts, which can ease mutual interference between the soil and structure. The SBFEM and meshless interface enables multilevel cross-scale modeling in the whole region (solid element and interface zone). In addition, the approach can simplify the process of local mesh optimization. Thus, the FEM-SBFEM-Meshless interface provides a competent tool for fine dynamic analysis in practical geotechnical engineering.

3.4. Simulating a three-arch type metro structure

In this section, the enhanced meshless interface is applied to a three-arch type metro structure for damage evolution analysis. The geometry of the typical three-arch type metro structure is shown in Fig. 28. The underground soil is 96 m long and 37.6 m deep. Depending on the application, the requirements placed on the properties of the mesh may cause the meshes of the soil and structure to restrict each other and forcing compromises in mesh quality. However, the coupled Meshless-SBFEM-FEM can avoid this issue by allowing highly effective independent meshing of model components. Similar to section 3.3, the soil and structure are meshed independently and connected by an enhanced meshless interface. The process of independent meshing is shown in Fig. 29.

The material parameters and ground motion inputs are same as with section 3.3 (frame metro structure). Four example states of tensile damage are shown in Fig. 30. From the results we can conclude that mild damage occurred initially at the bottom of each column before the tensile damage gradually reached 0.9 during the earthquake. Meanwhile, the tensile damage on both sub arches are pronounced at the regions at 30° to the vertical axis and is more severe compared with the slight damage of the main arch. In addition, regions at –30° angles with the vertical axis on both sub arches also experienced minor damage. After 20s when the input motion weakens, the damage distribution of the whole metro structure nearly remains constant. The distribution of damage is consistent with the simulation results in previous literature [48].

From this numerical example, we can summarize that the quad tree technique and the enhanced meshless interface simplify the process of mesh generation in complex regions. Meanwhile, we can conclude that the enhanced meshless interface is effective in simulating the circular (cambered) type soil-structure interaction. In addition, coupled with FEM and SBFEM, the enhanced meshless interface can precisely and flexibly simulate the evolution of damage in three-arch type metro structures.

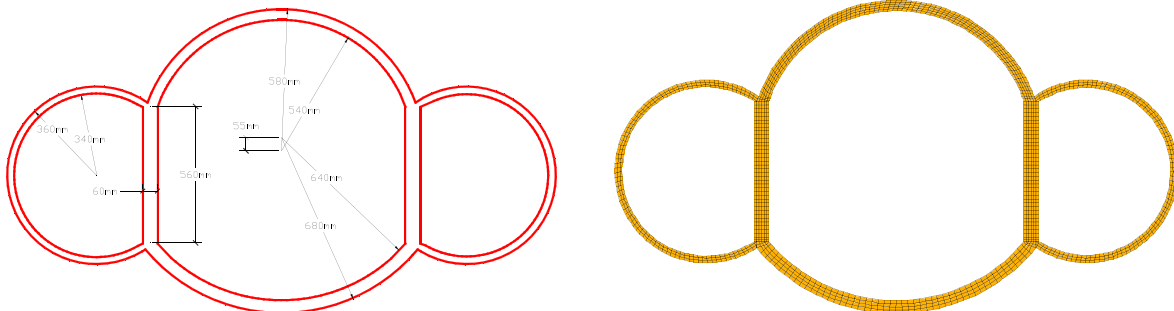


Fig. 28. The detailed size and meshes of a three-arch type metro structure.

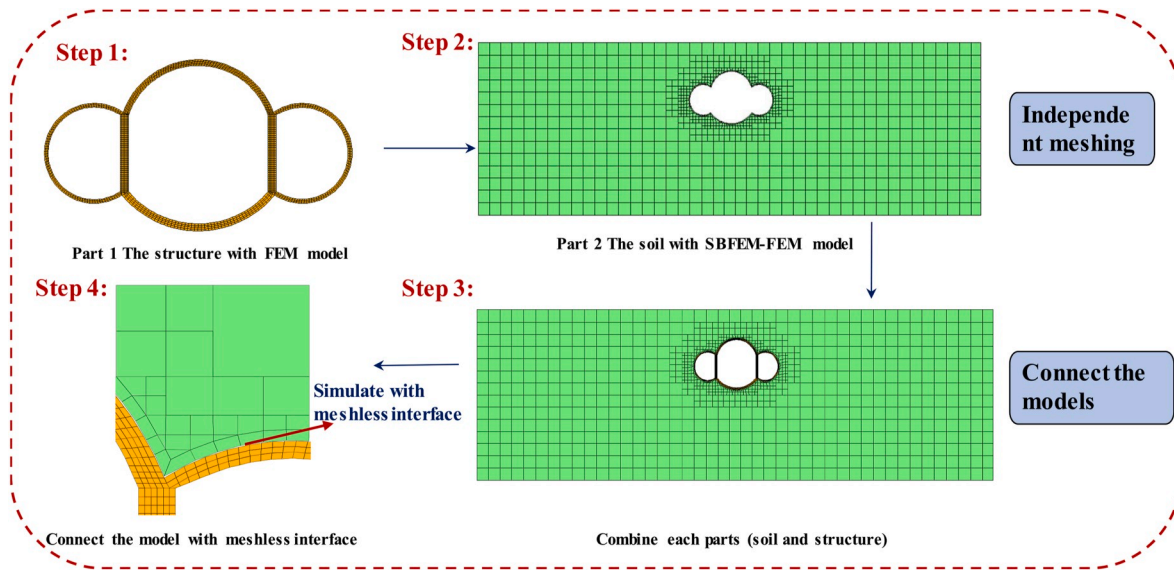


Fig. 29. The process of independent meshing.

4. Conclusions

This paper presents a coupled Meshless-SBFEM-FEM method to achieve multilevel cross-scale modeling especially for fine analysis in SSI problems. In addition, with the goal of overcoming the disadvantages of meshless interfaces, an enhanced meshless interface is presented. The enhanced meshless interface improves the accuracy near the boundary of interfaces and can be applied to simulate circular (cambered) type interfaces. Through object-oriented programming, the enhanced meshless interface and SBFEM are integrated into GEODYNA, which is a FEM framework. Thus, the introduced method can adopt advanced constitutive models in FEM to effectively simulate complex SSI problems. Finally, the Meshless-SBFEM-FEM is applied to the fine dynamic damage analysis of metro structures. Three preliminary conclusions can be

drawn as follows:

- (1) The coupled Meshless-SBFEM-FEM method can achieve the multilevel cross-scale model and enable fine analysis of the structure in SSI problems. The method can significantly reduce the number of elements and thereby increase the efficiency of computation. Furthermore, the introduced method can avoid the interference between soil and structure meshes and simplify the process of local mesh optimization.
- (2) The meshless interface and SBFEM take quite different approaches in solving shape functions, stiffness matrices, internal and external force vectors. In this paper, through object-oriented programming in C++, the SBFEM and meshless interface is integrated into a FEM framework. Following the steps delineated in

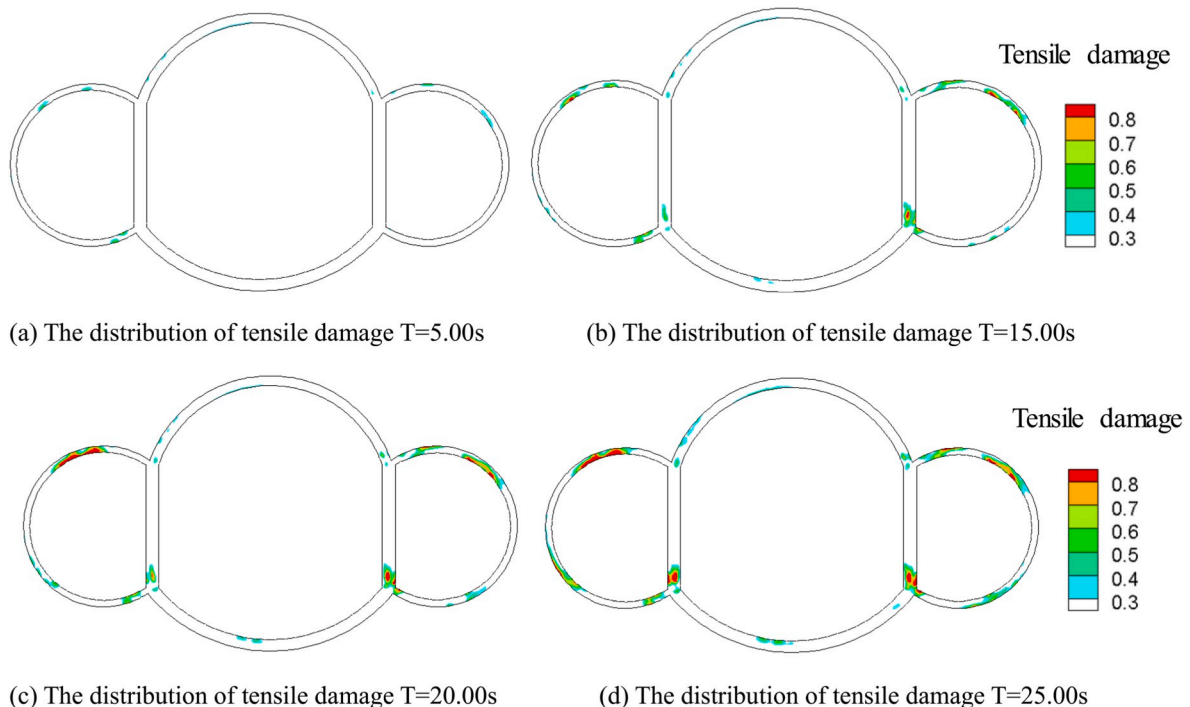


Fig. 30. Four typical time of tensile damage of three-arch type's metro structure.

this paper, readers can implement and reproduce the introduced method. The integrated method can directly handle various loads and constitutive models, thus vastly broadening the potential applications of the Meshless-SBFEM-FEM method.

- (3) The traditional meshless interface has lower precision near boundaries and can only be applied to straight lines or polyline type interfaces. The enhanced meshless interface developed in this paper extends the method to circular (cambered) type interfaces and improves the precision near boundaries. Two examples, including simulations of soil-footing interaction and buried pipes, are provided to demonstrate the advantage of the enhanced meshless interface.

The coupled Meshless-SBFEM-FEM method provides a highly versatile tool in performing fine analysis and is suitable for use in practical geotechnical projects, such as for the analyses of buried drainage culverts, concrete face rock-fill dams, etc. In future work, this method will be further developed to solve large deformation and saturated soil problems.

Declaration of competing interest

The authors declare that they have no known competing financial interests or personal relationships that could have appeared to influence the work reported in this paper.

CRediT authorship contribution statement

Jin Gong: Conceptualization, Methodology, Software. **Degao Zou:** Software, Validation. **Xianjing Kong:** Conceptualization, Resources. **Jingmao Liu:** Supervision. **Kai Chen:** Writing - review & editing, Project administration.

Acknowledgements

This work was supported by National Key R&D Program of China (Grant No. 2017YFC0307305), the National Natural Science Foundation of China (Grant Nos. 51890915, U1965206) and the Fundamental Research Funds for the Central Universities (Grant No. DUT19ZD216).

References

- [1] Anitescu M, Potra FA. Formulating dynamic multi-rigid-body contact problems with friction as solvable linear complementarity problem. *Nonlinear Dynam* 1997; 14:231–47.
- [2] Kausel E. Early history of soil-structure. *Soil Dynam Earthq Eng* 2010;30:822–32.
- [3] Goodman RE, Taylor RL, Brekke TL. A model for the mechanics of jointed rocks. *J Soil Mech Found Div* 1968;94:637–60.
- [4] Xu B, Zou DG, Kong XJ, et al. Dynamic damage evaluation on the slabs of the concrete faced rockfill Dam with the plastic-damage model. *Comput Geotech* 2015; 65:258–65.
- [5] Zhong H. Large-scale numerical simulation for damage prediction of high arch dams subjected to earthquake shocks [D]. PhD thesis. China: Dalian University of Technology; 2008.
- [6] Zhang Z, Liu Y, Dissanayake DD, et al. Nonlocal damage modelling by the scaled boundary finite element method. *Eng Anal Bound Elem* 2019;99:29–45.
- [7] Zhang J, Song C. A polytree based coupling method for non-matching meshes in 3D. *Comput Methods Appl Math* 2019;349(1):743–73.
- [8] Chen K, Zou DG, Kong XJ, et al. A novel nonlinear solution for the polygon scaled boundary finite element method and its application to geotechnical structures. *Comput Geotech* 2017;82:201–10.
- [9] Chen K, Zou DG, Kong XJ, et al. A nonlinear approach for the three-dimensional polyhedron scaled boundary finite element method and its verification using Koyna gravity dam. *Soil Dynam Earthq Eng* 2017;96:1–12.
- [10] Chen K, Zou DG, Kong XJ, et al. An efficient nonlinear octree SBFEM and its application to complicated geotechnical structures. *Comput Geotech* 2018;96: 226–45.
- [11] Zou DG, Chen K, Kong XJ, et al. An approach integrating BIM, octree and FEM-SBFEM for highly efficient modeling and seismic damage analysis of building structures. *Eng Anal Bound Elem* 2019;104:332–46.
- [12] Sharma KG, Desai CS. Analysis and implementation of soil-structure interface. *J Geotech Geoenviron Eng* 2004;130(8):851–60.
- [13] Desai CS, Ma Y. Modelling of joints and interfaces using the disturbed-state concept. *Int J Numer Anal Methods GeoMech* 1992;16(9):623–53.
- [14] Clough GW, Duncan JM. Finite element analyses of retaining wall behavior. *J Soil Mech Found Div* 1971;97(12):1657–73.
- [15] Liu H, Ling HI. Constitutive description of interface behavior including cyclic loading and particle breakage within the framework of critical state soil mechanics. *Int J Numer Anal Methods GeoMech* 2008;32(12):1495–514.
- [16] Hu LM, Pu JL. Application of damage model for soil-structure interface. *Comput Geotech* 2003;30:165–83.
- [17] Zou DG, Xu B, Kong XJ, et al. Numerical simulation of the seismic response of the Zipingpu concrete face rockfill dam during the Wenchuan earthquake based on a generalized plasticity model. *Comput Geotech* 2013;49:111–22.
- [18] Liu H, Song E. Seismic response of large underground structures in liquefiable soils subjected to horizontal and vertical earthquake excitations. *Comput Geotech* 2005; 32(4):223–44.
- [19] Yu X, Kong XJ, Zou DG, et al. Linear elastic and plastic-damage analyses of a concrete cut-off wall constructed in deep overburden. *Comput Geotech* 2015;69: 462–73.
- [20] Zou DG, Chen K, Kong XJ, et al. An enhanced octree polyhedral scaled boundary finite element method and its applications in structure analysis. *Eng Anal Bound Elem* 2017;84:87–107.
- [21] Xing W, Song C, Tin-Loi F. A scaled boundary finite element based node-to-node scheme for 2D frictional contact problems. *Comput Methods Appl Math* 2018;333: 114–46.
- [22] Xing W, Zhang J, Song C, et al. A node-to-node scheme for three-dimensional contact problems using the scaled boundary finite element method. *Comput Methods Appl Math* 2019;347:928–56.
- [23] Qu YQ, Zou DG, Kong XJ, et al. A novel interface element with asymmetric nodes and its application on concrete-faced rockfill dam. *Comput Geotech* 2017;85: 103–16.
- [24] Qu YQ, Zou DG, Kong XJ, et al. A flexible various-scale approach for soil-structure interaction and its application in seismic damage analysis of the underground structure of nuclear power plants. *Sci China Technol Sci* 2018;61:1092–106.
- [25] Gingold RA, Moraghan JJ. Smooth particle hydrodynamics: theory and applications to non-spherical stars. *Mon Not Roy Astron Soc* 1977;181:375–89.
- [26] Belytschko T, Lu YY, Gu L. Element-free Galerkin methods. *Int J Numer Methods Eng* 1994;37:229–56.
- [27] Jie Y, Tang XW, Luan MT, et al. Adaptive element free Galerkin method to analysis of earthquake induced liquefaction. *Earthq Eng Vib* 2008;7(2):217–24.
- [28] Liu GR, Gu YT. A local radial point interpolation method (LR-PIM) for free vibration analyses of 2-D solids. *J Sound Vib* 2001;246(1):29–46.
- [29] Liu GR, Gu YT. Coupling element free Galerkin and hybrid boundary element methods using modified variational formulation. *Comput Mech* 2000;26:166–73.
- [30] Liu GR, Gu YT. Comparisons of two meshfree local point interpolation methods for structural analyses. *Comput Mech* 2002;29:107–21.
- [31] Gong J, Zou DG, Kong XJ, et al. An extended meshless method for 3D interface simulating soil-structure interaction with flexibly distributed nodes. *Soil Dynam Earthq Eng* 2019;125.
- [32] Wang JG, Liu GR. A point interpolation meshless method based on radial basis functions. *Int J Numer Methods Eng* 2002;54:1623–48.
- [33] Wolf JP, Song CM. Finite-element modelling of unbounded media. Chichester: Wiley; 1996.
- [34] Wolf JP, Schanz M. The scaled boundary finite-element method. Chichester, U.K: Wiley; 2004.
- [35] Schauer M, Rodriguez GR. A coupled FEM-SBFEM approach for soil-structure-interaction analysis using non-matching meshes at the near-field far-field interface. *Soil Dynam Earthq Eng* 2019;121:466–79.
- [36] Estorff OV, Quan J. Direct coupling of EFGM-FEM and EFGM-BEM for dynamic soil-structure interactions. *Int J Numer Methods Eng* 2005;2(4):627–44.
- [37] Zhang X, Lu MW, Wegner JL. A 2-D meshless model for jointed rock structures. *Int J Numer Methods Eng* 2000;47:1649–61.
- [38] Bathe KJ, Chaudhary A. A Solution method for planar and antisymmetric contact problems. *Int J Numer Methods Eng* 1985;21(1):65–88.
- [39] Burns JW, Richards RM. Attenuation of stress for buried cylinders. *Proc symp on soil-structure interaction. Univ of Arizona*; 1964. p. 378–92.
- [40] Bandis SC, Lumaden AC, Barton NR. Fundamentals of rock joint deformation. *International journal of rock mechanics and mining science* 1971;12(8):1657–73.
- [41] Pastor M, Zienkiewicz OC. A generalized plasticity, hierarchical model for sand under monotonic and cyclic loading. *Proceedings of the 2nd international symposium on numerical models in geomechanics* 1986:131–50.
- [42] Liu JM, Zou DG, Kong XJ. A three-dimensional state-dependent model of soil-structure interface for monotonic and cyclic loadings. *Comput Geotech* 2014;61: 166–77.
- [43] Lee J, Fenves GL. Plastic-damage model for cyclic loading of concrete structures. *J Eng Mech* 1998;124(8):892–900.
- [44] Newmark NM. A method of computation for structural dynamics [C]. *American Society of Civil Engineers*; 1959.
- [45] Yoshida N, Kobayashi S, Suetomi I, et al. Equivalent linear method considering frequency dependent characteristics of stiffness and damping. *Soil Dynam Earthq Eng* 2002;22(3):205–22.

- [46] Chen GX, Chen S, Zou X, et al. Shaking-table tests and numerical simulations on a subway structure in soft soil. *Soil Dynam Earthq Eng* 2015;76:13–28.
- [47] Zhuang HY, Yang J, Chen S, et al. Seismic performance of underground subway station structure considering connection modes and diaphragm wall. *Soil Dynam Earthq Eng* 2019;127.
- [48] Chen GX, Chen S, Qi CZ, et al. Shaking table tests on a three-arch type subway station structure in a liquefiable soil. *Bull Earthq Eng* 2015;13:1675–701.